DELFT UNIVERSITY OF TECHNOLOGY

MSE THESIS REPORT
MS53035

Improving Performance Of Blades In EUV Lithography Machines

Author: Adithya Keshav Mohan
Student Number: 5522226

THESIS COMMITTEE:
Dr. Ir. Vera Popovich (Chair/Supervisor, MSE)
Dr. Poulumi Dey (MSE)
Andre Bras (ASML)

December 8, 2023

[This page was intentionally left blank]

ACKNOWLEDGEMENTS

I extend my heartfelt gratitude to my academic supervisor, Dr. Vera Popovich, whose unwavering guidance, scholarly insights, and invaluable feedback have been instrumental in shaping this thesis. Dr. Popovich's mentorship and dedication to my intellectual development have been a constant source of inspiration throughout this research journey. I would also like to express my sincere appreciation to Andre Bras, my company mentor, whose practical wisdom, industry experience, and constructive critiques enriched my understanding of real-world applications and enhanced the quality of this work. His commitment to bridging the gap between academia and industry has been truly commendable. My heartfelt thanks go to Sean Scott and Remko Seijffers, technicians at the materials science and engineering laboratory (TU Delft) whose technical expertise and unwavering support in the laboratory were pivotal in the successful execution of the experimental phase of this thesis. Both Sean's and Remko's contributions were indispensable in overcoming challenges and achieving the research goals. A special debt of gratitude is owed to Johannes Brouwer, a technician at the additive manufacturing laboratory (TU Delft), whose remarkable technical skills, innovative ideas, and collaborative spirit significantly contributed to the experimental setup and the generation of novel concepts during this project. Without his tireless efforts and enthusiastic brainstorming sessions, the completion of this project would have been an insurmountable task. I am also deeply indebted to my family for their unwavering support, patience, and encouragement throughout this thesis project. Their constant belief in my abilities and sacrifices made this endeavor possible. In addition, I wish to acknowledge the unyielding support of my friends, Harshraj Gali and Georgiy Pissarev, who stood by me during moments of uncertainty, offering both moral and intellectual support. Your friendship provided much-needed respite during the demanding times of research and writing. Furthermore, I extend my thanks to ASML for offering me the opportunity to undertake my thesis project within their esteemed organization. This experience was invaluable in gaining practical insights into the industry and conducting research with real-world implications. Finally, I acknowledge the contributions of the Materials Science and Engineering department at TU Delft for providing the necessary equipment, facilities, and academic environment conducive to research. The department's resources played a significant role in the successful execution of my project. This thesis represents the culmination of the collective efforts and support of these individuals, and I am profoundly grateful for their contributions to my academic and personal growth.

Adithya Keshav Mohan
Delft, December 2023

ABSTRACT

Ceramics are being explored as an alternative material by ASML to replace their stainless steel 316L (SS316L) reticle masking blades. Ceramics offer distinct advantages over stainless steel in the semiconductor industry. While stainless steel exhibits good mechanical strength, ceramics excel in electrical insulation and thermal conductivity, making them essential for semiconductor manufacturing. Ceramics, with their lower thermal expansion coefficient, enhanced chemical stability, lightweight nature, and dielectric properties, are essential for improving the performance, miniaturization, and reliability of semiconductor devices. This research addresses the challenge of replacing the SS316L blades in ASML's EUV lithography reticle masking with high-purity alumina (99.7%) through binder jetting. Concurrently, emphasis was placed on optimizing the existing REMA blade design for the binder jetting technique. This research further assesses the thermo-mechanical performance of the new blade suggesting the necessity of cooling channels in the new blades. High-purity alumina was chosen for its superior material properties compared to SS316L. The research also focuses on analyzing the impact of particle size, printing parameters, and sintering conditions on the densification and mechanical properties of binder-jetted alumina samples. Unimodal 20 µm, unimodal 10 µm, and trimodal (equal concentrations of 10, 5, and 2 µm) powder batches were printed using binder jetting. The trimodal samples with 90% binder saturation exhibited the best results in green body density (61.3%) and sintered body density (66.9%). The Young's modulus and flexural strength achieved by the trimodal sample was also the highest with a value of 77.3 ± 4.9 GPa and flexural strength of 59.5 ± 3.2 MPa. To enhance densifications further, it is recommended to incorporate sintering additives in the powder mixture and/or utilize nanoparticle densifiers in the binder. Additionally, employing the discrete element method using smaller particles with a multimodal powder mixture is also recommended for achieving higher densification.

NOMENCLATURE

3D	Three Dimensional
Al	Aluminum
AlN	Aluminum Nitride
ALPS	Activated Liquid Phase Sintering
AM	Additive Manufacturing
BC	Boundary Conditions
BJ	Binder Jetting
BJP	Binder Jetting Printer
CIM	Ceramic Injection Molding
CTE	Coefficient of Thermal Expansion
DC	Direct Current
DEM	Discrete Element Method
disp.	Displacement
DOF	Depth of Focus
DUV	Deep Ultraviolet
DUVL	Deep Ultraviolet Lithography
EDS	Energy-Dispersive X-Ray Spectroscopy
EUV	Extreme Ultraviolet
EUVL	Extreme Ultraviolet Lithography
F	Fine
FEA	Finite Element Analysis
HTC	Heat Transfer Coefficient
IUPAC	International Union of Pure and Applied Chemistry
LPS	Liquid Phase Sintering
Max.	Maximum
ME	Material Extrusion

MLC	Multilayered Ceramic Circuits
NA	Numerical Aperture
PBF	Powder Bed Fusion
PSD	Particle Size Distribution
PSPS	Pressureless Spark Plasma Sintering
REMA	Reticle Masking
SEM	Scanning Electron Microscope
Si	Silicon
SiC	Silicon Carbide
SiSiC	Siliconized Silicon Carbide
SPS	Spark Plasma Sintering
Temp.	Temperature
TRI-70	Trimodal with 10 µm, 5 µm, and 2 µm alumina powder mixed at equal concentrations with 70% binder saturation
TRI-90	Trimodal with 10 µm, 5 µm, and 2 µm alumina powder mixed at equal concentrations with 90% binder saturation
UNI-10	Monomodal 10 µm alumina powder
UNI-20	Monomodal 20 µm alumina powder
XF	Extremely Fine
XRD	X-Ray Diffractometry

CONTENTS

LIST OF FIGURES

LIST OF TABLES

CHAPTER 1

INTRODUCTION

In the past 50 years, the semiconductor industry has revolutionized microchips, making them smaller, denser, and more powerful. They follow Moore's law [1], which states that the computer's speed, measured by the number of transistors placed on a microchip, doubles every two years. Currently, almost tens of billions of transistors are used in a single microchip. The manufacturing of microchips is a complex process and incorporates photolithography technology [23]. Photolithography is a projection system where light is projected through a 'mask' or 'reticle' which contains the blueprint of the pattern that is to be printed on a photosensitive silicon wafer. The pattern is encoded in the light and using the optical system in the machine, the encoded pattern is shrunk and focused onto the wager. According to the Rayleigh diffraction effect (Equation 1.1), the reduced feature sizes in a microchip can be achieved by using a smaller wavelength of light. The numerical aperture also plays a crucial role as it defines how much light the optics can collect. The Rayleigh criterion can be defined as:

$$R = k_1 * \frac{\lambda}{NA} \quad [23] \tag{1.1}$$

Where:
R → Resolution (smallest feature size) or critical dimension
k_1 → Resolution factor
λ → Wavelength of the light source
NA → Numerical aperture

The state-of-the-art techniques used in manufacturing microchips are deep ultraviolet lithography (DUVL) and extreme ultraviolet lithography (EUVL). DUVL defines patterns in a thin photosensitive polymer called a photoresist with the wavelength of the light source ranging from 254-193 nm [9]. The EUVL light source has a wavelength of 13.5 nm [74], which is currently the leading-edge technology. The EUVL technique helps with printing really fine features on the microchips making the chips cheaper, high-performing, high processing power, and less energy consuming. The next-generation extreme ultraviolet (EUV) platform will also have a higher NA from 0.33 to 0.55 [59], therefore enabling even finer features to be printed. This literature review will focus on the EUVL technology.

ASML is currently the only company with cutting-edge EUVL technology leading the semiconductor industry. ASML has collaborated with TU Delft and designed a Master's graduation project with the main focus of determining possible replacement of the stainless steel blades with a ceramic material used in the reticle module for their EUVL system.

1.1 Thesis Objective

The manufacturing workflow for the stainless steel reticle masking blades in ASML's EUV machines is characterized by a highly intricate process, encompassing multiple suppliers and critical steps, resulting in low yield rates and significant cost implications. This thesis project is centered on the exploration of a potential alternative material, with a specific emphasis on ceramics, owing to their exceptional thermal properties. The primary objective is to assess the feasibility of manufacturing ceramic components using the binder jetting technique. Among the various ceramic materials under consideration, alumina has been selected as the focal point of this study due to its widespread usage in the industry. The selection of binder jetting as the prospective manufacturing technique for alumina is motivated by its capacity to produce large-scale components with high precision. Furthermore, this thesis endeavors to attain high-density ceramic components by optimizing both printing and post-processing parameters. The existing ASML reticle masking blades are also to be optimized for binder jetting manufacturing. Thermo-mechanical simulations are to be conducted to verify the compatibility of the ceramic materials given ASML's requirements.

1.2 Thesis Outline

The thesis is structured into six chapters. Chapter 1, "Introduction," serves as the opening chapter, delineating the scope and purpose of the thesis project, and presenting the overarching research objectives. Chapter 2, "Background and Literature Study," delves into the foundational knowledge required for the comprehension of the thesis, providing a comprehensive overview of relevant literature. It also includes a detailed case study on the application of binder jetting technology to alumina materials. Chapter 3, "Materials and Methods," carefully explains the materials used in the experiments and describes the methods and techniques employed in the research. In Chapter 4, "Results and Discussion," the experimental findings are presented and analyzed in detail. Finally, Chapter 5, "Conclusions," summarizes the key findings, draws overall conclusions, and offers insights into potential future directions and recommendations resulting from the thesis project. This structured framework facilitates a systematic and comprehensive exploration of the research, allowing for a logical progression of ideas throughout the thesis.

CHAPTER 2

BACKGROUND AND LITERATURE STUDY

2.1 EUV Lithography

EUVL is the next-generation lithography method that incorporates the usage of radiation of wavelength near 13.5 nm to imprint the patterns from a reflective mask (reticle mask) onto a wafer substrate coated with a photoresist which is a light-sensitive material. The whole process occurs under vacuum conditions in an all-reflective optics configuration [13]. It is important to maintain the vacuum conditions as the short EUV wavelength (13.5 nm) is absorbed by most materials [6]. This technology is used to manufacture integrated circuits (ICs) wherein the print features are smaller than 32 nm. The projection lens system used in EUVL reduces the mask pattern by a factor of four onto the photoresist [55]. The critical dimensions of the print features are defined by the lithography process while other processes are defined in other procedures such as etching, ion implantation,*etc.* The capacity to print the smallest feature is described through Equation 1.1. Depth of focus (DOF) is also another important factor in determining these features. It can be defined as:

$$DOF = \pm k_2 * \frac{\lambda}{NA^2} \quad [62] \tag{2.1}$$

Where:
DOF → Depth of focus
k_2 → Proportionality factor (constant)

The smallest feature that can be printed in the semiconductor industry has followed the trend wherein the number of transistors used in an IC is doubled every two years [50]. This trend is called Moore's law.

Figure 2.1 shows the schematics of EUVL with the projection optical system based on reflective mirrors [54].

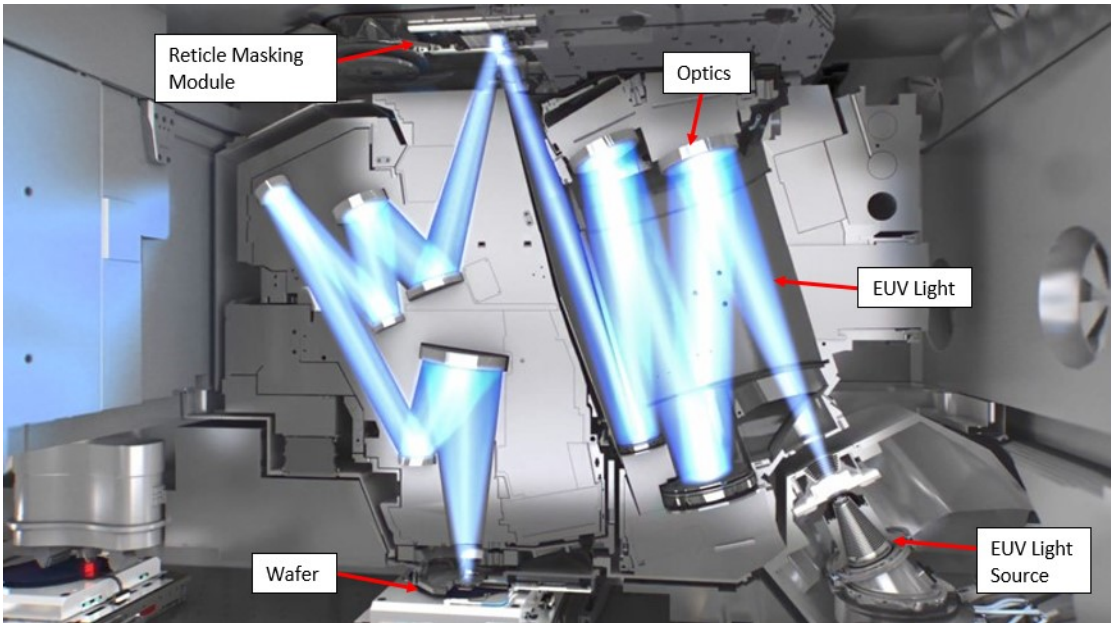

Figure 2.1: Schematics of EUVL [54]

2.2 Reticle Masking

The reticle masking (REMA) module in an EUV system contains the blueprint of the pattern that is to be imprinted onto the wafer substrate. Light is projected through this 'mask' or 'reticle', therefore the mask has to have reflective properties and should not absorb the short wavelength of light, this makes it different when compared to the traditional transmissive optical masks. The pattern is encoded in the light which is then processed through the system's optics which then shrinks and focuses the pattern on the photosensitive substrate. Each layer of the reticle mask represents different layers of the device, therefore, they cannot be made identical [27].

REMA blades are included in the reticle to block any additional radiation outside the active printing region [29]. The light impinged on the REMA blades is absorbed while the light impinged on the exposed regions of the reticle is reflected back onto the substrate.

2.3 Ceramics

Ceramics broadly describes materials made from non-metallic, inorganic compounds heated to high temperatures [7]. It can also be defined as "the art and science of making and using solid articles which have their essential component and are composed in large part of, inorganic nonmetallic materials" [35]. The word "ceramic" is derived from the Greek word "keramos," which means "potter's clay." Ceramics are usually associated with a combination of different bonds like covalent, ionic, and sometimes metallic. They do not contain any discrete molecules and consist of arrays of interconnected atoms. Ceramics are mostly compounds of metals or metalloids and nonmetals. They are typically oxides, nitrides, and carbides, however, diamonds and graphites are also classified as ceramics. Based on the definition a material is no longer considered to be a ceramic when it is melted. On the other hand, ceramics become superconductors when they are sufficiently cooled [10].

Ceramics offer several advantages in EUV applications compared to other materials. Their unique combination of properties makes them well-suited for various EUV applications, enabling improved performance, reliability, and longevity of EUV systems. Ceramics exhibit high-temperature stability which allows them to withstand the high temperatures that the REMA blade is exposed to in the EUV system. This property makes ceramics maintain their structural integrity and functionality even under extreme thermal conditions. For example, aluminum nitride has a thermal conductivity in the range of 192 - 208 W/m°C whereas stainless steel 316L has a thermal conductivity of only 16 W/m°C which is lesser by a factor of 12. Ceramics also have a low coefficient of thermal expansion which is a crucial characteristic in EUV applications where dimensional stability is required to maintain the accuracy and performance of EUV systems. For example, alumina has a CTE in the range of 8.7 - 9.1 µstrain°C whereas stainless steel 316L has a CTE of approximately 15.5 µstrain°C which is more than 2 times than that of alumina. Ceramics also have low-outgassing properties, meaning that they release minimal amounts of volatile compounds or gases when exposed to vacuum conditions. Since the REMA blades are exposed to vacuum conditions, the environment is required to be clean and particle-free for efficient propagation of EUV light, this makes ceramics ideal candidates. In EUV applications, where components come into contact with intense energy and high-energy particles, ceramics can provide robust protection against wear, abrasion, and damage caused by these interactions. Ceramics also exhibit high dielectric strength and low electrical conductivity. Certain ceramics have good optical transparency (for example, alumina) in the EUV range. This is very crucial because EUV systems require precise control and transmission of EUV light for the patterning and imaging processes.

2.3.1 Classification of Ceramics

Ceramics are classified based on atomic and structural arrangement. They can be classified as monolithic and composite ceramics. Monolithic ceramics are further classified into crystalline solids and amorphous. Crystalline solids are subdivided into single crystals and polycrystals. Amorphous materials are categorized into glasses and other solid materials except for glass. Figure 2.2 shows a schematic representation of the classification.

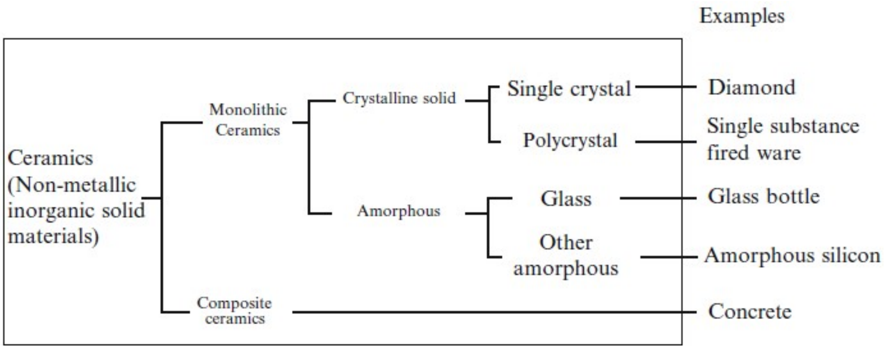

Figure 2.2: Classification of ceramics [32]

In ceramics, the atoms are bonded together. In crystalline solids (Figure 2.3), the atoms are periodically arranged following a particular order throughout the material. Examples of crystalline solids include porcelain, precious stones, and pottery. Amorphous (non-crystalline) on the other hand does not have any long-range order, however, they have homogeneous attributes with an irregular atomic arrangement (Figure 2.3). An example of amorphous is glass.

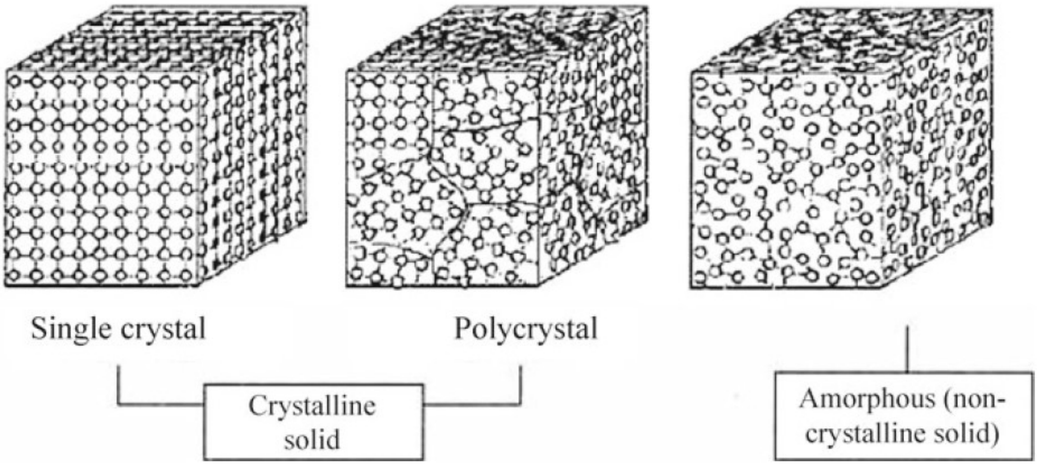

Figure 2.3: Structure of ceramics [32]

Single crystals have periodically arranged atoms from one end to the other end of the material where grain boundaries are absent. Although the atoms are arranged periodically in single crystals, the properties may vary based on the direction of the arrangement (anisotropy). Polycrystals consist of many grains wherein the adjacent grains usually have different orientations. They are typically manufactured in a high-temperature furnace through the process of sintering forming "sintered bodies." These sintered bodies have various grain orientations and the properties are not determined based on the direction [32].

Glasses are special ceramics, typically manufactured by melting silicates at high temperatures and then quenching them. The molten glass has high viscosity below its solidification temperature (supercooled condition), therefore preventing the formation of crystals. As the temperature decreases the viscosity increases and the material transforms into glass near the glass transition temperature. At this point, there is no free movement of the atoms, therefore, making it a thermodynamically unstable state and favoring crystallization at room temperature. The time taken for a glass to undergo crystallization is extremely long and therefore can be used without any concerns. Overall, any material that exhibits a glass transition state can be defined as glass. Amorphous solids other than glass also have a homogeneous atomic arrangement without any periodicity or regularity in a wide range. During manufacturing, they do not undergo the supercooling process or pass through the glass transition phase [32].

Composite materials are a combination of multiple chemical compounds, metals, and polymers. Each phase in a composite represents a substance present in the composite. Composite materials consist of one or more phases that are distinguished from the matrix. Composites are advanced materials that are made by the combination of various industrially-produced high-purity raw materials [32]. Ceramics are often used as reinforcements in many composites.

2.3.2 Types of ceramics

Ceramics are a diverse class of materials that offer a range of properties and applications. Ceramics can be categorized based on their composition, properties, and applications. Traditional ceramics are the most widely used ceramics. They typically constitute natural materials like clay minerals, quartz sand, and feldspar. They are known for their high compressive strength, low tensile strength, and excellent resistance to heat, abrasion, and chemical attack [58]. They are typically used to make clay bricks, tiles, china tableware (whiteware), refractory linings, and pottery.

Advanced ceramics (or technical ceramics) are engineered for specific design requirements usually made by synthetic chemicals of high impurity [58]. They can be tailor-made with multiple functionalities. They exhibit superior properties with regard to mechanical, electrical, optical, magnetic, and corrosion resistance [10]. They are divided according to the non-metallic composition (oxides, carbides, and nitrides). They are used in a range of applications like piezoelectric components, aerospace, ceramics for dynamic random access memories (DRAMs), *etc.*

Refractory ceramics are materials that do not physically or chemically change at high temperatures and harsh environments [61]. They have an upper hand when it comes to withstanding high degrees of thermal and mechanical stresses as well as high resistance to corrosion [63]. They are typically used as furnace linings, kiln furniture, and glass-making crucibles.

Bioceramics are materials that are typically used in medical applications for musculoskeletal restoration [57]. Bioceramics interact with the surrounding tissues while also providing support for tissue growth [70]. They are usually made from synthetic or natural raw materials that are compatible with human tissue. Bioceramics have high strength and hardness amongst other mechanical properties [72]. They can also bond with bone and tissue. They are used in applications of load-bearing bone and tissue implants, porous scaffold materials, dental implants, joint replacements, *etc* [51].

Table 2.1 showcases examples of ceramics belonging to various ceramic groups. The examples provided offer a glimpse into the diverse range of ceramics utilized in different industries.

Table 2.1: Examples of ceramics in different ceramic groups

Ceramic Group	**Examples of Ceramics**
Traditional Ceramics	Porcelain, Earthenware, Stoneware, Terra Cotta, Whiteware
Advanced Ceramics	Alumina (Aluminum Oxide), Zirconia (Zirconium Oxide), Silicon Carbide, Silicon Nitride, Boron Nitride, Titania (Titanium Dioxide), Aluminum Nitride
Refractory Ceramics	Magnesia, Chromite, Zircon, Mullite, Silica, Alumina-Silica, Alumina-Zirconia, Silicon Carbide, Graphite, SiSiC (Siliconized Silicon Carbide)
Bioceramics	Hydroxyapatite, Bioactive Glass, Zirconia, Alumina, Calcium Phosphate, Bioglass, Bioceramic composites

2.4 Microstructures of Ceramics

This section will cover an overview of some of the microstructures observed in ceramics.

2.4.1 Crystalline Structure

Ceramics are typically composed of crystalline structures which can be determined through the atomic and ionic arrangement in space. The crystal structures have a huge impact on the material properties. Some of the major crystal structures include cubic, tetragonal, orthorhombic, monoclinic, and triclinic [35]. Ceramics like diamond and perovskite have a cubic structure that consists of an equal-length unit cell along the three axes making 90°angles between these axes. Ceramics like zirconia and barium titanate have tetragonal structures which consist of unit cells with the two perpendicular axes having unequal lengths and the third axis having equal lengths. Ceramics like alumina and calcium tungstate have an orthorhombic structure which has a unit cell with unequal lengths along all three perpendicular axes. Ceramics like potassium niobate and strontium titanate have a monoclinic structure which has a unit cell with two unequal lengths along the two perpendicular axes and the third axis makes an inclined angle with the other two axes. Ceramics like pyroxene and kyanite have a triclinic structure that has a unit cell with unequal lengths along all three axes with unequal angles between them [35].

2.4.2 Grain Structure

The polycrystalline structures of ceramics consist of various grains that are formed during the processing of ceramics. The grain size also impacts the strength of the polycrystalline ceramics as observed through the Hall-Petch equation. The strength decreases as the grain size increases [10]. The toughness also decreases with increasing grain size due to the increase in the number of grain boundaries. The grain structure of ceramics affects their properties and performance in various applications. Therefore, it is essential to understand the different grain structures that can be observed in ceramics and how they affect the material's properties to optimize their microstructure for specific uses. Ceramics can display different grain structures that depend on how they are processed and what their composition is. They typically exhibit equiaxed grains, columnar grains, and/or lamellar grains.

Equiaxed grain structures are microstructures that are roughly equal-sized in all directions (2.4-a). Due to the equiaxed structure, the stresses are more evenly distributed thereby improving the material properties [34]. Columnar grain structures are microstructures that are elongated (column-like shape), with their axes oriented along a preferred direction. Columnar grain structures are often exhibited by ceramics that are produced through techniques such as directional solidification or zone melting (2.4-b). The rate of solidification and temperature gradient determines the orientation and growth of the grains [12]. The columnar grain structure can influence the ceramic material's mechanical, thermal, and electrical properties. For example, the mechanical strength and fracture toughness are enhanced by providing a preferred direction for crack propagation, also improvising the load-bearing capacity along the grain direction. Lamellar grain structures are microstructures with their grains oriented in a plate-like pattern and have a layered structure in their crystallographic orientation (2.4-c). These structures are typically observed in ceramics that undergo deformation, re-crystallization, or phase transformation [14]. Similar to columnar, lamellar grain structures also influence the ceramic material's mechanical, thermal, and electrical properties.

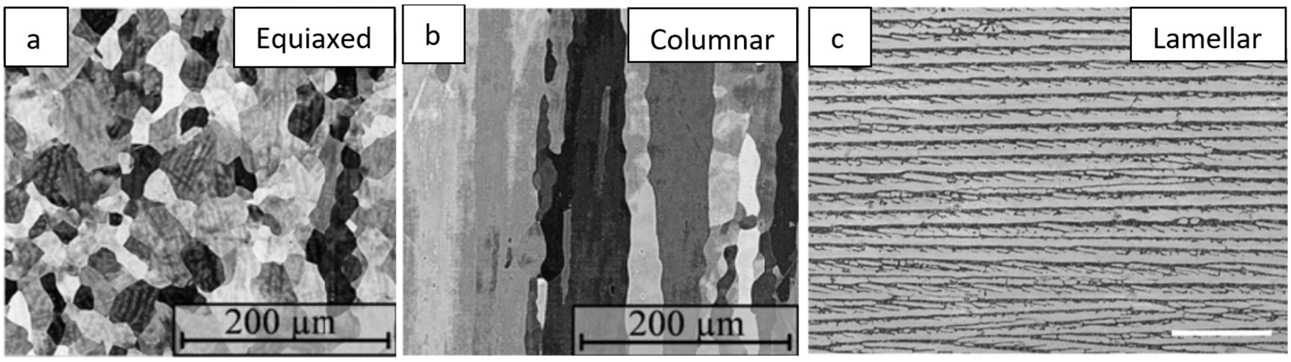

Figure 2.4: SEM micrograph showing: (a) Equiaxed grain structure [39], (b) Columnar grain structure [39], (c) Lamellar grain structure [73]

Controlling the grain size and its distribution during the sintering process is crucial as these factors affect the material properties like porosity and density. Adjusting the grain boundary migration also helps in controlling the grain size as they are closely related. Appropriate material composition and sintering conditions can result in obtaining the ceramic material with the specific grain size and density requirements [75].

2.4.3 Porosity

The International Union of Pure and Applied Chemistry (IUPAC) defines porosity as the percentage found by dividing the total space volume (cell cavities) by the bulk volume [69]. In other words, they are the voids or "empty spaces" within the ceramic material. The presence of pores impacts the material properties (physical, chemical, and mechanical) of the ceramic material. Generally, the increase in porosity decreases the strength and hardness exponentially as described by the Ryshkewitch equation (Equation 2.2). Ceramic materials have volatile components like water present in them and when they go through shrinkage during the sintering process these components are released and voids are created in their place within the material [75]. The presence of pores in ceramics can be both beneficial and detrimental. For example, pores can make the material lighter, a good energy absorber, *etc.*, however, they can also cause the material to be more brittle and weak. Various manufacturing processes can control the porosity in the material thereby enabling the optimization of material properties depending on the desired application. Adjusting the composition of the raw materials and the additives used can also influence the degree of porosity [57]. Introducing certain additives prevents the re-crystallization process and thereby removes the pores through the grain boundaries [75].

$$\sigma = \sigma_0 * e^{-cp} \quad [58] \tag{2.2}$$

Where:
$\sigma \rightarrow$ Strength of the material
$\sigma_0 \rightarrow$ Strength at zero porosity
c → constant
p → porosity

2.4.4 Intergranular Phase

Intergranular phase (or grain boundary phase) are materials that are located between the intersection of grains in ceramic materials [15]. Intergranular phases are formed either during the processing of ceramics and/or the introduction of additives or impurities. Similar to the other microstructures, this phase also impacts the material properties significantly. The intergranular phase consists of glassy and amorphous materials like alumina and/or silica. They bind the grains together thereby increasing the toughness and strength of the ceramic material. Optimizing the intergranular phase is essential in obtaining the desired material properties. The liquid phase that occurs during the sintering process, especially due to the addition of sintering additives, forms an amorphous intergranular phase upon cooling [77]. This weakens the ceramic material and deforms at higher temperatures due to the softening of intergranular phases (low softening point) [45]. According to Guo *et al.* [24], the change in volume that is caused by the crystallization of the amorphous intergranular phase introduces residual stresses which as a result impact the strength at higher temperatures. Therefore, adjusting the additive amount would be essential in decreasing the presence of an amorphous intergranular phase.

2.5 Manufacturing Methods of Ceramics

Efficient and defect-free manufacturing of 3D advanced ceramic parts is a complex undertaking due to the unique properties of these materials. Processing ceramics from the molten state is extremely challenging given the high melting temperature and low ductility of advanced ceramics. Additionally, their poor thermal shock resistance often leads to crack and pore formation, which occurs when forming parameters and temperature treatments are not precisely controlled [41]. Furthermore, the high hardness and brittleness of advanced ceramics make the machining of ceramics (post-sintering) challenging and often results in defects and surface microcracks. Machining can also be expensive primarily due to the use of diamond cutting and grinding tools.

These challenges are typically overcome by processing ceramic powders. Ceramic powders are typically mixed with a binder, deflocculant, and plasticizer to create a dry powder mix. This mix is then shaped into the green body through techniques like die pressing or cold isostatic pressing. Alternatively, ceramic powders can be dispersed in a liquid carrier to form a ceramic slurry for tape casting or slip casting, or combined with wax for injection molding [41]. Dry forming processes are more commonly used in industry due to their cost-effectiveness, although wet forming techniques are employed when dry forming is insufficient.

After forming, the organic binder is removed using a debinding process, leaving behind a "brown" body. This body is then subjected to sintering at an elevated temperature (typically between 50-90% of the melting temperature of the ceramic material), which triggers a physicochemical transformation, resulting in the formation of the desired ceramic component with the required properties and microstructure [41]. Additional post-processing steps, such as machining, grinding, and polishing, may be required to achieve the desired surface finish and dimensional accuracy.

The following sections provide an overview of diverse manufacturing techniques employed in the production of ceramics.

2.5.1 Tape Casting

Tape casting is a manufacturing method that is used to produce thin layers of ceramic. These thin layers can later be stacked and laminated into multi-layer structures. Tape casting is typically used to produce capacitors, multilayered ceramic circuits (MLC), solid fuel cells, *etc.* In this method, the ceramic slurry is carefully spread onto a surface using a controllable casting blade (called a doctor blade) [30]. The ceramic slurry is mainly composed of powder, which determines the properties of the product along with other ingredients that impact the rheological behavior of the slurry [30]. A solvent is used to form the fluidity of the slurry and create a homogeneous mixture of all the ingredients used in the slurry. Additive agents called surfactants (SURFace ACTive AgeNT) are also used in the slurry to obtain the desired characteristics of the particle surface. These additives also influence specific properties such as sintering behavior, thermal expansion, conductivity, and sometimes color. Binders are used in the slurry to keep the powder in a certain shape until it is heated to an appropriate temperature where the powder is sintered together to achieve the final properties. Plasticizers or sintering agents are also added to help in casting the product along with improvising their mechanical properties or physical properties [30]. After milling all these agents together, the homogenized slurries are then laid onto the casting film machine which forms green sheets that are laminated and stacked together to form the green body. Figure 2.5 shows the schematics of the tape casting process.

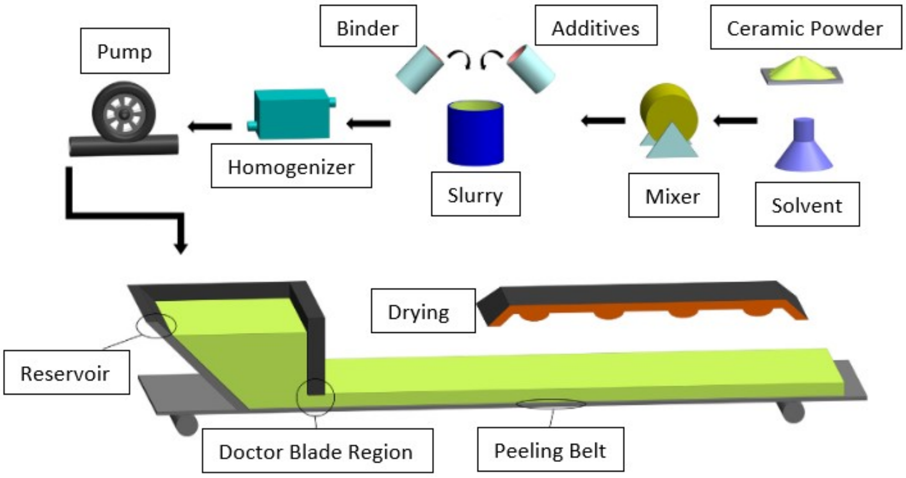

Figure 2.5: Schematic representation of the tape casting process [30]

2.5.2 Slip Casting

Tape casting is a manufacturing method where aqueous suspensions called slips (or slurries or dispersions) are poured into a porous mold made of plaster which absorbs moisture from the slip and solidifies the material to form the desired shape of the object. The slip is a mixture of water, organic dispersants, a blend of ceramic powder materials, surfactants, plasticizers, and binders [71]. This method is usually used to fabricate components that are medium or large in size. Slip casting is typically used to produce complex shapes like whiteware (plates, bowls, cups, sinks, bathtubs *etc.*, and art pottery. They are also used to produce technical ceramics such as insulators, bearings, and other electronic components. A significant advantage of slip casting is that it can be used to produce complex shapes with high levels of accuracy. Figure 2.6 shows the schematics of the slip-casting process.

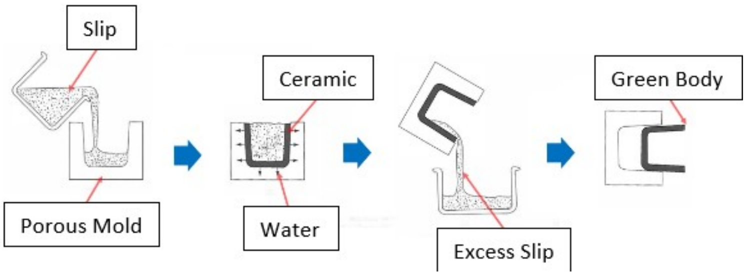

Figure 2.6: Schematic representation of the slip casting process [66]

2.5.3 Ceramic Injection Molding (CIM)

CIM is a manufacturing method that helps produce three-dimensional components in high volume. It is a variation of plastic injection molding which incorporates ceramic powder and thermoplastic binder material. The major advantage of CIM is that this method can help produce parts with complex shapes in one step while maintaining the net-shape quality [71]. The mixture of ceramic powder and binder material is heated to form a slurry which is then injected into a mold to create the desired shape of the object. The slurry inside the mold is heated to higher temperatures in order to melt and evaporate the binder material forming a solid ceramic part. The mold is typically made of steel or aluminum. Figure 2.7 shows the schematics of the CIM process.

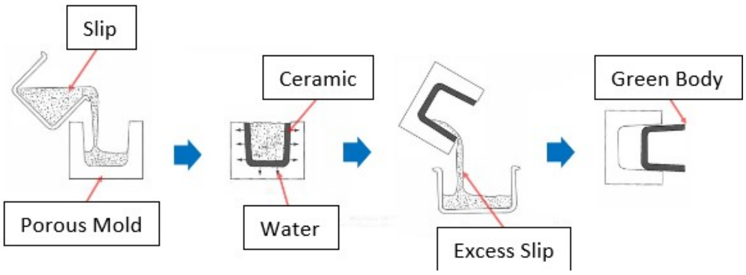

Figure 2.7: Schematic representation of the ceramic injection molding process [52]

2.5.4 Ceramic Extrusion

Ceramic extrusion is a process where the ceramic paste is extruded through a shaped die at a continuous length under high pressure. The ceramic paste is a mixture of ceramic powder, binders, plasticizers, along with other additives. The extruded material is cut into appropriate lengths and then sintered. Ceramic extrusion is typically used to produce large parts with complex shapes with high precision [26]. Figure 2.8 shows the schematics of the ceramic extrusion process.

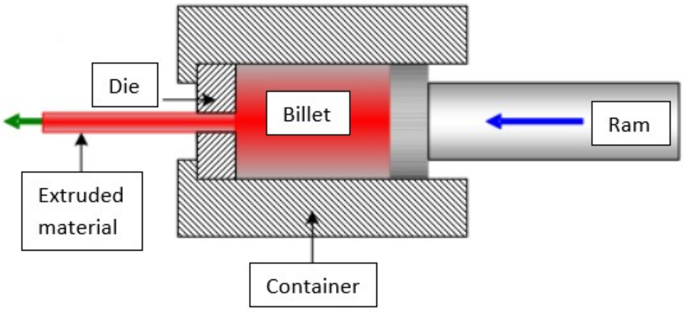

Figure 2.8: Schematic representation of the ceramic extrusion process [38]

2.5.5 Ceramic Pressing

Ceramic pressing is a forming process that involves compressing the ceramic material into the desired shape using a mold and high pressure. Typically, there are four major types of pressing; dry-pressing, semi-dry pressing, wet-pressing, and isostatic pressing. Dry pressing incorporates axial compaction of granulated ceramic dry powders which are pressed into a mold using a die/punch arrangement [44]. The ceramic powder is mixed with a binder material which holds the powder particles together. The binder material is then evaporated during the sintering process. Dry-pressing is typically used for producing simple shaped parts and small parts with high precision and a good surface finish without the need for any additional processing steps [53]. Figure 2.9 shows the schematics of the ceramic dry-pressing process.

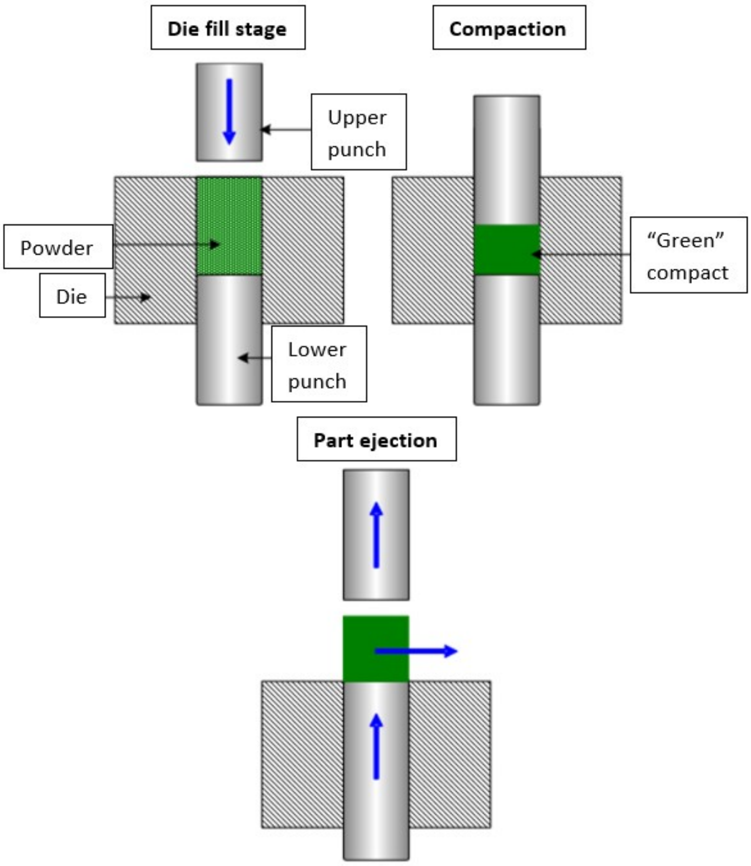

Figure 2.9: Schematic representation of the ceramic dry-pressing process [38]

Semi-dry pressing process is a combination of both dry-pressing and slip casting process. It incorporates a mixture of dry and wet ceramic powder to form a slurry which is pressed into a mold to form the desired shape using a die. Semi-dry pressing is typically used for producing parts with complex shapes, high precision, good surface finish, and offer better moisture control [64].

Wet-pressing incorporates a mixture of ceramic powder and a liquid binder forming a slurry which is poured onto a mold and pressed using a hydraulic press. The excess liquid is thereby removed and a partially dried green body is formed [36]. Wet-pressing is typically used for producing parts with complex shapes with high density thus having better mechanical properties and performance. Figure 2.10 shows the schematics of the ceramic wet-pressing process.

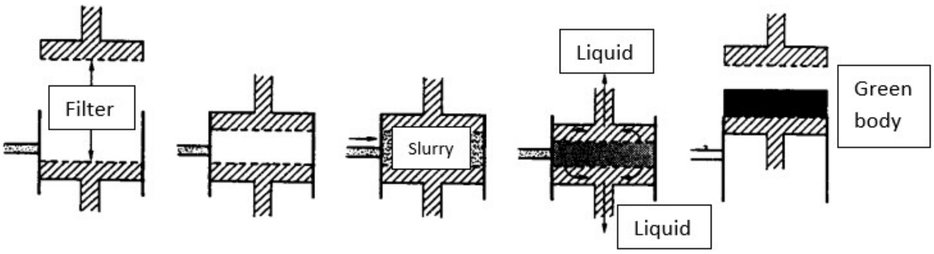

Figure 2.10: Schematic representation of the ceramic wet-pressing process [36]

Isostatic pressing is a manufacturing process where uniform pressure is applied on all sides of the mold under hydrostatic conditions [22]. The mold is filled with ceramic powder and is submerged in a fluid medium, typically water or oil. The pressure created using the hydrostatic pressure thus compresses the ceramic powder forming the desired shape of the part. Isostatic pressing is typically used to produce parts with complex shapes with high precision, high strength, and high density while maintaining uniform properties throughout the part [43]. Figure 2.11 shows the schematics of the ceramic isostatic pressing process.

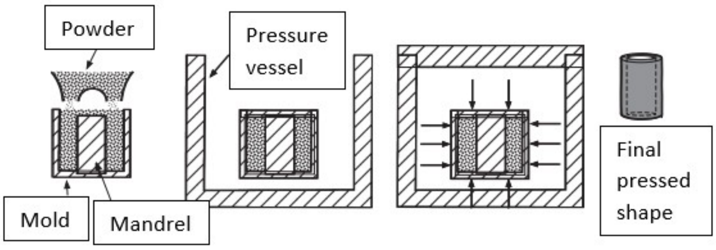

Figure 2.11: Schematic representation of the ceramic isostatic pressing process [22]

2.5.6 Spark Plasma Sintering

Spark plasma sintering (SPS) is a powder metallurgy technique that allows the compaction of ceramic materials (and powdered metals) and densifies the materials. This technique incorporates pulsed direct current (DC) and applies uniaxial pressure simultaneously onto the material, achieving the sintering process. The powder compact is loaded between the two electrodes (typically graphite), and this assembly is placed in the pressure die (typically graphite), which is electrically conducting [60]. Current is passed through the electrodes, which discharges high-temperature plasma (spark) at the contact points between the particles, encouraging localized heating to reduce the overall energy consumption. During this process, surface impurities, oxide layers, and absorbents present on the surface of the powder particles are removed and eliminated as residual products. Pressure is also simultaneously applied along with the current which rapidly heats and densifies the powder compact through atomic diffusion [46]. The SPS technique enhances control over the microstructure of the sintered material, thus controlling the grain distribution and grain size which helps in improving the material properties. SPS also helps in minimizing porosity, thus resulting in improved material properties. Compared to other conventional methods, SPS enables rapid heating rates, resulting in shorter processing times. Figure 2.12 shows the schematics of the SPS process.

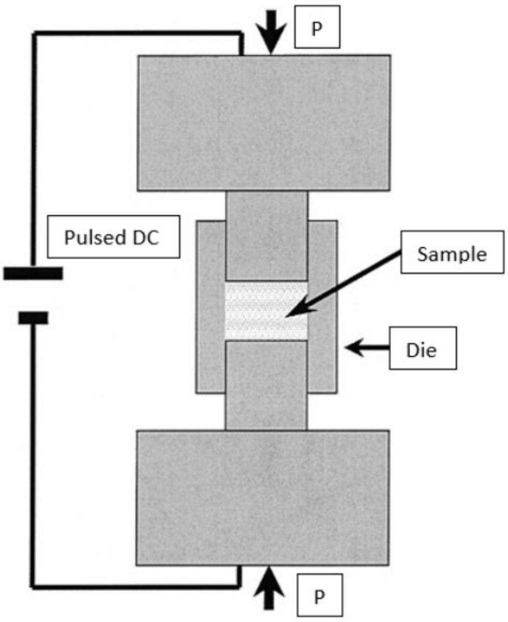

Figure 2.12: Schematic representation of the spark plasma sintering process [60]

2.5.7 Additive Manufacturing of Ceramics

Additive Manufacturing (AM), often called 3D printing, is a process wherein the ceramic material(s) is deposited layer-by-layer to create a 3D object from computer-based 3D model data [41]. AM provides an alternative approach to traditional forming processes for producing the 3D part without incorporating any expensive tooling.

In the ceramics industry, AM can economically produce prototypes, low-volume productions, and customized parts without the requirement for expensive dedicated mold tooling. In conventional manufacturing, the high cost of molds used in injection molding necessitates large production volumes to offset the tooling expenses. Additionally, design modifications and functional prototypes are constrained in conventional processes, as each iteration requires the fabrication of a new mold, resulting in time and cost implications [41]. Conversely, AM allows for easy design modifications by simply updating digital design files, involving changes in build orientation and processing parameters. The overall manufacturing cost in AM is primarily determined by the material used, power consumption of the machine, and cost of labor, while design complexity plays a minor role. In contrast, conventional processes like injection molding tie manufacturing costs to design complexity. This distinction is a key aspect supporting the use of ceramics in AM. There are several techniques involved in AM, however, for ceramic AM there are three major techniques; powder bed fusion, material extrusion, and binder jetting.

Laser-Based Powder Bed Fusion

Powder bed fusion (PBF) is an AM process that utilizes laser beams (laser sintering machines), which act as a thermal source to induce fusion between the powder particles. Additionally, electron beams or other thermal sources can be used, but it requires a significantly different machine architecture. The thermal source selectively sinters (or melts) the powdered material which is fused to the previous layer thus building the desired part layer-by-layer. PBF is highly suitable for ceramics given its brittle and hard nature [56]. The ceramic powder is prepared and loaded into the reservoir which spreads the powder evenly onto the build plate. A leveler blade is used to ensure uniform layer thickness. The powder is then sintered layer-by-layer as the build plate lowers to produce the desired part. This process is typically used to produce parts with complex geometries in small batch sizes and has an overall improvement in mechanical properties compared to the conventional manufacturing process. A major disadvantage is that it is challenging to obtain uniform powder distribution resulting in uneven properties. The parts also have to go through post-processing, which can be expensive and time-consuming. Figure 2.13 shows the schematics of the laser-based PBF process.

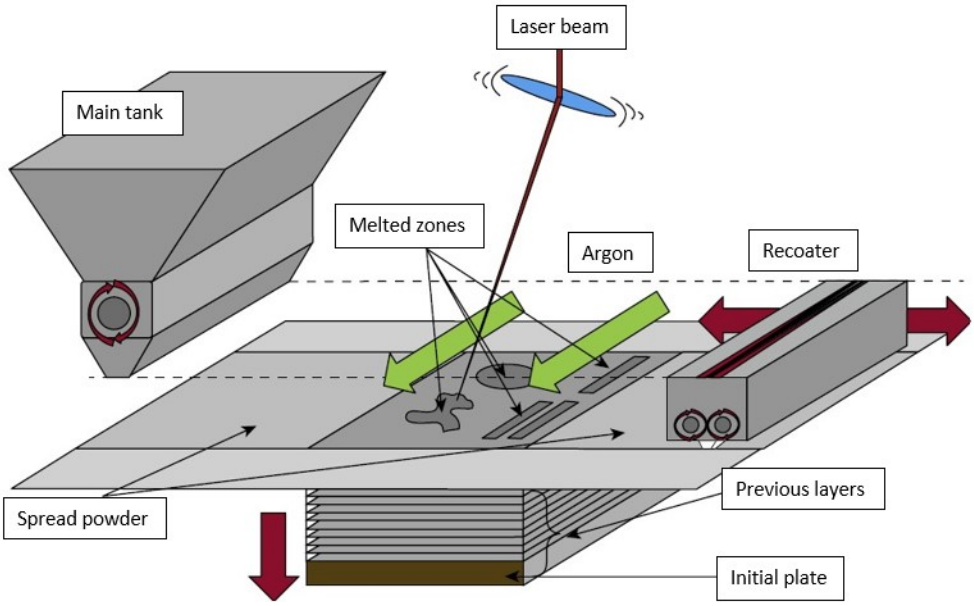

Figure 2.13: Schematic representation of the laser-based powder bed fusion process [65]

PBF of ceramics involves a range of important process parameters that significantly impact the printing process and the quality of the resulting ceramic parts. The power of the laser beam used plays a crucial role as it heats up and fuses the ceramic powder particle. Optimizing the power will ensure sufficient energy transfer and the proper melting of the ceramic particles [65]. The scan speed also influences the input energy and the dwell time in each area. Optimizing this parameter based on the ceramic used can yield the appropriate amount of sintering and minimize any damages that occur due to excessive heat. Layer thickness also plays a crucial role as it impacts the resolution and surface roughness of the printed part. How the laser scans across the powder also make an impact as it defines the pattern and the printing sequence [65]. It also affects the mechanical properties, surface finish, and build time of the parts, therefore optimizing this can yield uniform energy distribution and minimizes the thermal stresses. The spot size of the laser used impacts the accuracy and resolution of the printed part because it determines the complexity of the designed part and the spatial resolution.

The powder bed temperature can also have a significant impact on the sintering process and print quality. Therefore optimizing the preheating of the powder bed and maintaining the temperature throughout the process can ensure proper flowability and the degree of powder consolidation [65]. The characteristics of the ceramic powder such as particle size, distribution, shape, and flowability also significantly affect the packing density and the ability to achieve proper fusion during sintering. Lastly, the gas used in the build chamber can also impact the sintering process and the print quality. Typically, inert gases like argon are employed to prevent oxidation and maintain thermal conditions during the sintering process [65].

Material Extrusion

Material extrusion (ME) is an AM process that involves depositing the ceramic material (in the paste or slurry form) through an extruder (or nozzle) onto the build plate layer-by-layer to create a 3D object [56]. The ceramic powder in slurry (or paste) form is mixed with binders and loaded into the reservoir. The ceramic paste is extruded through the nozzle layer-by-layer, thus creating the desired object (green part). The green part is then heated in order to remove the binder and goes through a sintering process where the ceramic particles are sintered together. Material extrusion is typically used to produce parts with complex geometries with high accuracy and resolution and improve the mechanical properties of the part. This technology can also be used to produce in small batches. Major disadvantages include not being able to achieve uniform material properties and the limited range of materials that be used in this method due to their rheological properties. Similar to the powder bed fusion process, post-processing is also involved in the material extrusion process, which can be expensive and time-consuming. Figure 2.14 shows the schematics of the material extrusion process.

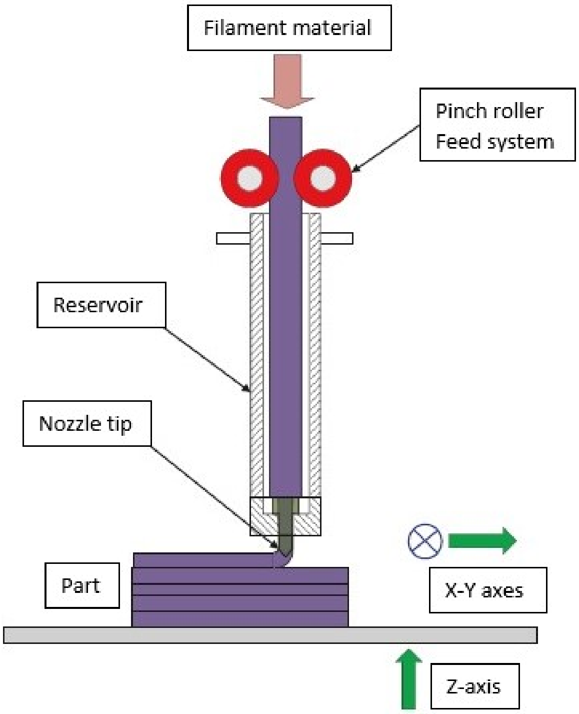

Figure 2.14: Schematic representation of the material extrusion process [56]

ME of ceramics involves several important parameters that significantly influence the printing process and the printed part. The properties of the ceramic paste used for extrusion such as viscosity, thixotropy, shear thinning behavior, and rheological characteristics, are of utmost importance for printability and obtaining quality parts [25]. These properties dictate the flow behavior and extrudability of the paste. The extrusion temperature also plays a crucial role in achieving the desired consistency and extrudability of the ceramic paste. Optimal results can be seen if the temperature is optimized based on the ceramic material that is being used. Another important parameter is the extrusion speed and pressure as they govern the rate of paste deposition through the nozzle [25]. These parameters directly impact the deposition accuracy, layer uniformity, and overall part quality. Finding the right balance between the extrusion speed and pressure is essential to minimize issues like nozzle clogging and ensure consistent material flow. The extrusion nozzle also plays a huge role in achieving quality parts and it is important to use a nozzle with appropriate size and geometry. The nozzle diameter determines the extrusion width, while the nozzle shape influences the deposition characteristics and, consequently, the resolution and surface quality of the printed parts [25].

The layer thickness, or extrusion height, is another parameter of significance. It determines the vertical resolution and surface roughness of the printed parts [25]. Choosing an appropriate layer thickness is essential to balance the printing speed and part quality. Thinner layers provide higher resolution but may increase printing time, while thicker layers reduce printing time at the potential cost of surface quality [25]. Should the part that needs to be printed require support (based on design complexity), it is important to select the appropriate material can also impact the stability and ease of its removal.

After printing, post-processing steps such as drying and curing are often necessary to remove the excess moisture from the part which in turn helps in increasing the strength of the material. Optimizing the temperature, time, and humidity parameters can help improve the part quality. Additionally, optimizing the debinding parameters (debinding time, temperature, and atmosphere) and sintering parameters (sintering temperature, heating rate, and holding time) can ensure the proper removal of binders and achieve the desired densification and mechanical properties.

Binder Jetting

Binder jetting (BJ) is an AM process wherein the ceramic powder is uniformly spread on a build plate and the binder material is selectively jetted onto the powder bed thereby binding the ceramic particles together layer-by-layer to create a 3D object [56]. The binder material (liquid form) is dispensed through the inkjet printhead. The powder bed (build plate) is lowered and a new layer is spread onto the previous layer and the next layer is printed. This process is repeated until the desired object (green part) is created. The green part is then removed from the powder bed and goes through post-processing to produce the final part. Binder jetting is typically used to produce complex shaped parts with high accuracy and resolution. The process has a relatively low impact on the environment compared to conventional methods. However, the mechanical proprieties of the final part are inferior, the porosity is higher and the surface finish is rougher compared to the conventional methods [11]. Figure 2.15 shows the schematics of the binder jetting process.

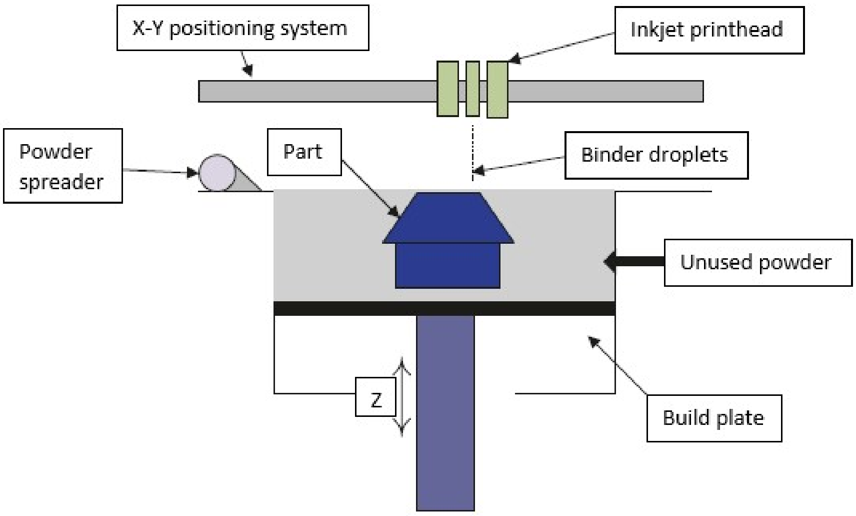

Figure 2.15: Schematic representation of the binder jetting process [56]

BJ of ceramics involves several important parameters that significantly influence the printing process and the printed part. Selecting an appropriate binder is crucial given its rheological properties like viscosity and surface tension which are critical in accurate deposition and effective infiltration of the ceramic powder [18]. The characteristics of the powders such as the particle size, shape, and distribution have a substantial impact on the printability and final quality of the printed parts. They also affect powder flowability, packing density, and sintering behavior [18]. Powder flowability is essential for the even distribution of powder layers during the printing process. The layer thickness plays a vital role in determining the resolution and surface quality of the printed part. This makes it important to carefully consider the appropriate layer thickness to achieve the desired detail and minimize visible layer lines or defects.

Another important factor is the binder dispensing parameters such as droplet size, spacing, and saturation, which are essential for achieving accurate binder deposition and uniform infiltration throughout the ceramic powder bed [18]. The energy source employed to selectively bind the ceramic powder layers together, significantly influences the consolidation mechanism, process speed, and efficiency. Post-processing processes such as debinding and sintering are essential parameters for achieving the final properties of the ceramic part. Optimizing the debinding parameters (debinding time, temperature, and atmosphere) and the sintering parameters (sintering temperature, heating rate, and holding time) is crucial to ensure proper binder removal and to achieve the desired densification and mechanical properties of the final ceramic part [18].

The orientation of the printed part and the design of support structures are also crucial parameters as they impact dimensional accuracy, surface finish, and buildability. Optimizing these parameters also minimizes defects like distortion, warping, and removal of extensive supports [18]. Lastly, another important parameter is the printing speed and the resolution, finding the optimal balance between both is critical to ensure the desired part quality [56].

2.6 Sintering

Sintering is the densification process of the ceramic powder at a high temperature just below the melting point of the material [75]. In this process, the particles are fused together forming a solid material. Sintering is a crucial process in the production of ceramic due to its impact on material properties. It can eliminate the pores from the green body, compress the residual pores, increase the binding amongst the grains, encourage grain growth, and improve the overall strength and hardness of the material. Figure 2.16 shows schematics of the sintering process. There are four types of sintering mechanisms; gas phase sintering, solid phase sintering, liquid phase sintering, and activated liquid phase sintering [75]. Each of these mechanisms has a different mass transfer mechanism for which energy is required.

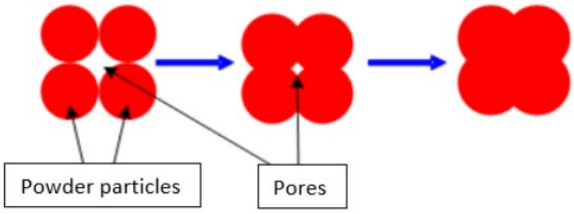

Figure 2.16: Schematic illustration of the sintering process. [37]

Gas phase sintering is a process wherein the ceramic powder is placed in a sealed container with a gas atmosphere, and this container is heated at high temperature and pressure resulting in the fusion of the ceramic particles. The driving force of this process is the differentiation in the vapor pressure [75]. The mass transfer is completed through evaporation and agglomeration. This process helps in reducing the oxidation of the ceramic material due to the presence of the gas atmosphere. It also enhances the material's strength and density. This process also encourages the uniform distribution of the particles resulting in obtaining a homogeneous object.

Solid phase sintering is a process wherein the ceramic powder is heated at a high temperature just below its melting point without any external force or pressure resulting in the fusion of the ceramic particles. The driving force of this process is the differentiation in free energy or chemical potential between the free surface of the particle and its interface with the neighboring particle [75]. The mass transfer is completed through diffusion wherein the atoms or vacancies are migrating along the surface, interface, or within the material body. During the sintering process, the ceramic particles are rearranged and bonded together at specific points resulting in the formation of necks which increase in size as the temperature rises. The mechanical properties of the ceramic material increase in this process due to the growth of large grains present within the material.

Liquid phase sintering (LPS) is a process wherein a small amount of additive that forms a small amount of liquid phase between the grains is added to the ceramic powder mixture prior to the sintering process [53]. The ceramic mixture is heated at a high temperature just below the melting point of the liquid phase which promotes the densification of the particles by melting and infiltrating the spaces present between these particles. The liquid phase surrounding the particles will generate capillary pressure which helps in solidification [75]. Therefore, capillary pressure and surface tension are the driving forces for this process. The mass transfer mechanisms in this process are the viscous flow of the liquid phase and diffusion. This process is strongly dependent on temperature as it is directly proportional to the amount of liquid phase produced. This process can enhance the densification rates, can produce specific grain boundary properties, or achieve accelerated grain growth [53].

Activated liquid phase sintering (ALPS) is a process wherein small amounts of eutectic-forming additives are added to the ceramic powder mixture are sintered resulting in enhanced densification rates observed before the eutectic temperature is reached when compared to the pure powder [53]. Compared to LPS, the concentration of the activated system is smaller in ALPS. The additive material can be composed of a metal, a metallic compound, salt, or a glass-forming material. The ceramic powder mixture is heated at a high temperature just below the melting point of the additive. The additive promotes the densification of the ceramic particles. During the sintering process, the liquid phase melts and diffuses into the ceramic powder which fills the pores between the ceramic particles. The liquid phase can still remain as a secondary phase or as a residual liquid or can totally disappear at the end of the sintering process after it is diffused completely [75]. The driving forces are the same as LPS while the mass transfer mechanisms are viscous flow, dissolution, and separation. This process can help reduce the sintering temperature due to the heat generated when the reactive material and liquid phase react with one another. Like the other sintering processes, this process also enhances the mechanical properties of the ceramic material.

Table 2.2 summarizes the sintering mechanisms discussed above.

Table 2.2: Sintering mechanisms [75]

Sintering type	**Mass transfer mechanism**	**Driving force**
Gas phase	Evaporation, Agglomeration	Differentiation in vapor pressure
Solid phase	Diffusion	Differentiation in free energy, Differentiation in chemical potential
Liquid phase	Viscous flow, Diffusion	Capillary pressure, Surface tension
Activated liquid	Viscous flow, Dissolution, Separation	Capillary pressure, Surface tension

2.7 Failure Mechanisms

Ceramics fail in various ways depending on the composition, microstructure, and external loading conditions.

2.7.1 Fracture

In ceramics, fractures occur generally due to discontinuities in the microstructure, which are small cracks that are distributed in the surface or volume [16]. This suggests that the strength of the material varies from component to component and depends on the size of the largest defect in that specimen or the most critical defect. Therefore, a large number of specimens is required to find the strength distribution. The loading of the component and the stress field influences the macroscopic occurrence of fractures. Ceramics show brittle characteristics in low and ambient temperatures. They are typically triggered by the normal tensile stresses in the component. In the brittle fracture of ceramics, certain characteristics are commonly observed. Fracture origin is considered to be a critical flaw as it behaves like a crack. Initially, during the crack extension, the crack path is typically observed to be perpendicular to the first principal stress. The fracture origin is surrounded by regions called mirror, mist, and hackle. Figure 2.17 shows these regions on a forced rupture of a silicon nitride valve that has undergone a tensile test. The size of the fracture origin, mirror, and mist is typically proportional to σ^{-2}, where σ, represents the stress in an uncracked body at the fracture origin.

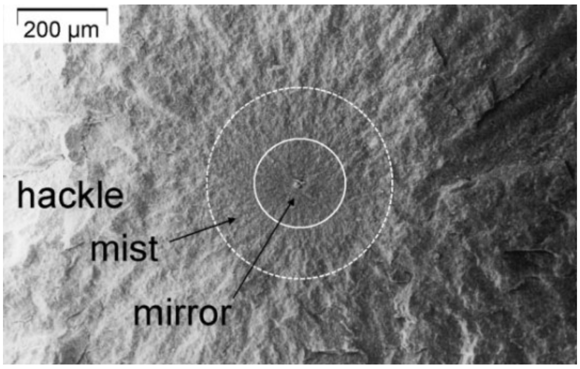

Figure 2.17: Fracture mirror, mist, and hackle on the fracture surface of a silicon nitride valve [16]

Amongst various failure modes, thermal shock, and contact loading play a huge role in the appearance of macroscopic fractures. Thermal shock failure occurs when the temperature changes rapidly, causing thermal gradients and thermal strains within the material. This results in crack propagation and encourages failure. Cooling shock is a type of thermal shock, where for example, a heated material is quenched and the heat is transferred to the environment through the surface of the material, thereby attempting to shrink. The interior of the material is still at a higher temperature compared to its surface, this causes tensile stresses in the surface region. Cracks can be observed when the tensile stresses reach a critical value. Figure 2.18 shows an example of thermal shock that occurred due to quenching in PTC ceramics. When stresses exceed critical levels (locally), thermal shock cracks occur. These cracks reduce the tensile stress around them, which diminishes the driving force for further crack extension, stopping crack propagation. The direction of the crack is opposite to the heat flow. [16]

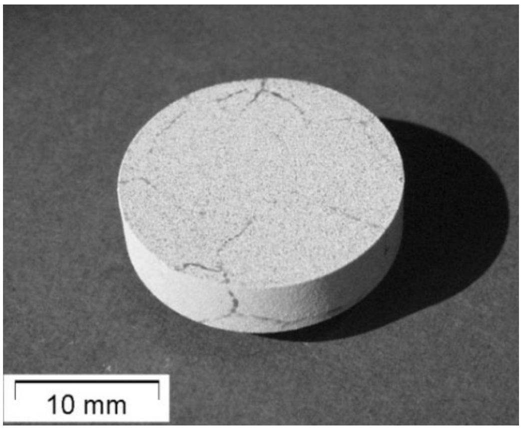

Figure 2.18: Thermal shock cracks in quenched specimens of PTC ceramics [16]

When hard surfaces are in contact with one another, either through static or dynamic impingement, it can lead to cracks if the stresses exceed critical values. Contact damages do not typically result in immediate failure, however, it can serve as an origin for delayed failures when cracks grow over time. There are two major types of contact damage; blunt contact and sharp contact.

Blunt contact occurs when a sphere contacts a flat surface which causes an elastic deformation, resulting in the formation of a circular contact area. Within this area, compressive stresses occur wherein the magnitude of these stresses increases with applied load and decreases with the sphere radius. Significant tensile stresses occur in the narrow ring-shaped region around the contact zone. The formation of a ring-shaped crack called the Hertzian ring crack (Figure 2.19-a) occurs when these tensile stresses exceed a critical value [16]. As the tensile stresses decrease rapidly below the surface, it usually prevents the cracks from penetrating deeply. However, with the increase in loading, the cracks tend to extend obliquely at an angle of 22° from the indented surface resulting in the formation of a cone-shaped crack. Hertzian cracks are often caused due to improper handling and/or localized overload. These cracks can be well modeled using Brinell hardness testing as they are blunt indentation techniques.

Sharp contacts, on the other hand, is a point loading situation that results in a severe plastic deformation beneath the contact point, resulting in the formation of radial cracks (Figure 2.19-b). Such cracks are typically observed at sharp features like the corners of the indentation marks. High internal stresses are generated through plastic deformation, influencing the development of cracking and damage [42]. Lateral cracks are typically formed below the plastically deformed region and extend parallel to the surface. During the wear of ceramics, a common mechanism that is observed is the breaking of large fragments or chips of material, this is typically a result of lateral cracks intersecting with the radial cracks and the surface [16]. These cracks can be well modeled using Vickers or Knoop hardness testing as they are sharp indentation techniques.

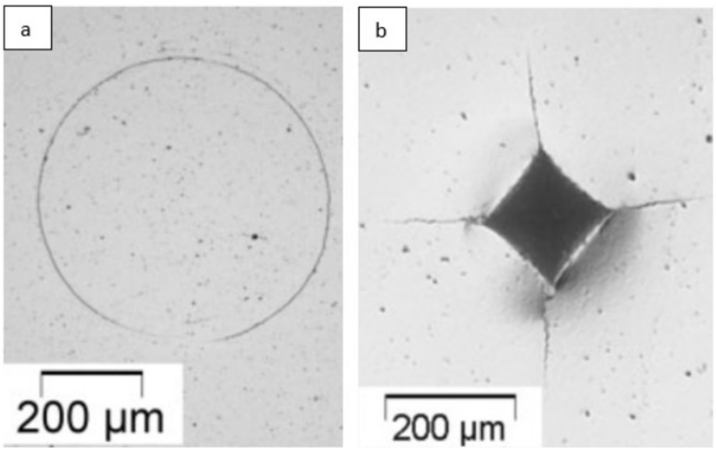

Figure 2.19: Contact damages: (a) Hertzian ring crack in silicon nitride sample (b) Radial cracks in silicon nitride at the edge of Vickers indent [16]

2.7.2 Fatigue

In ceramics, failures due to fatigue are also typically observed. Fatigue failure is the progressive degradation and eventual fracture of ceramic materials typically due to cyclic loading on a material below its fracture strength [32]. Cyclic loading results in stress concentration within the material which in turn results in the formation of microcracks or defects within the material. These usually occur at particular locations that are associated with imperfect surfaces, grain boundaries, or other structural irregularities. The microcracks tend to grow and propagate due to the progressive cyclic loading as it generates alternating stress. The propagation of these cracks is influenced by several factors such as stress intensity (increased load frequency), crack geometry, and material properties. As the crack tends to grow, they eventually merge with neighboring cracks leading to the formation of larger cracks and reducing the load-bearing capacity of the material. Eventually, these cracks reach a critical size which leads to a catastrophic failure.

2.8 Binder Jetting of Alumina

Being one of the most used ceramics, α-alumina is employed for its various functional properties as described in 4.1.3. According to previous studies, achieving a full-density alumina component is highly challenging. Table 2.3 highlights various densification strategies adopted. The cases seen in Table 2.3 were not significant in achieving high-density alumina. A computer-based simulation study was performed by Mariani *et al.* to understand the packing efficiency of two pure α-alumina powders given their size distribution [48]. The two α-alumina powders were:

- 99.8% purity - extremely fine (XF) Al_2O_3 powder (CT530SG) with a declared powder size (D_{50}) of 1.7 µm.
- a 99.8 % purity - gas atomized fine (F) Al2O3 spherical powder (DAM10) with a declared D_{50} of 9 µm.

The printer used was an Innovent Plus 3D printer by ExOne (Huntington, PA, US), and the binder used during the printing process was a commercial water-based product (BA-005). The powder batches were thermally treated (at 200°C for 5 hours in the air) prior to printing in order to remove the residual humidity and eliminate any agglomerates present as it could hinder the spreading of the powder on the powder bed. The initial printing was done to study the printing parameters. A layer thickness of 50 µm was maintained throughout the study in order to avoid any losses due to geometrical resolution. Binder saturation considered were 55% and 75%. The specimen geometries that were considered for the bending tests were cubes (27 mm^3) and parallelepiped with dimensions (length = 31.75 mm; width = 12.70 mm; height = 6.35 mm). Volatile binder solvents were removed by initially curing the printed components at about 180 °C for 6 hours in the air; this also promoted the polymerization of the residual component. Later the component went through the debinding process where it was heated to about 470°C for 30 minutes in the air with a heating rate of 5°C min^{-1}. Optimal sintering parameters were identified by thermally treating the samples, featuring two cycles with different parameters as seen in Table 2.4. The study also analyzes the evolution of relative densities through the heat treatment processes. The study also includes the measurements of the flexural strength (FS) of the parallelepiped samples using the ASTM C1161-18 standard (3-point bending test) for both the green and sintered components. This method involved the calculation of the flexural mechanical resistance using Equation 2.3. The flowability of both powders is determined using the Hausner index (H) using Equation 2.4. Table 2.5 summarizes the values obtained for both the α-alumina powders.

Table 2.3: Binder Jetting of alumina [48]

Powder Size (D_{50}) [µm]	**Layer Thickness [µm]**	**Binder Saturation [%]**	**Green Density [%]**	**$T_{sintering}$ [°C]**	**$t_{sintering}$ [h]**	**Sintered Density [%]**
53	26/53/106	60	-	1600	2 16	60-65
45	23/45/90					75-85[1]
30	15/30/60					80-95[1]
Mixed	15/45/106					90-96[1]
60	500	-	45	1600	2	48
2	130	-	-	1600	2	46.8
10						57.5
70						60.5
10+2						50.7
70+10						64.8
70+2						64.3
70+10+2						65.5
20+3.4+0.4	-	-	39.0	1500	5	-
40	-	-	50.7-65.7	-	-	-
33	100	90	45	-	-	-
0.8 +18.5	100	110	-	1200	2	34.4
45+6	110	-	21.7-43.9	1650	2	67.8
0.3	120	-	6	1600	2	32
73.9			15.8			50.7

[1] Relative density values of sintered components may have been overestimated due to measurement with Archimedes' method of samples with open porosity not sealed correctly (as suggested by SEM images).

Table 2.4: Thermal treatment parameters [48]

Cycle	**Heating ramp [°Cmin]**	**$T_{sintering}$ [°C]**	**$t_{sintering}$ [h]**
A	5	1550	3
B	2	1750	3

$$FS = 3PL/(2bd^2) \quad [48] \tag{2.3}$$

Where:
P → Break load (N)
L → Support span (mm)
b → Specimen width (mm)
d → Specimen thickness (mm)

$$H = \rho_{tap}/\rho_{app} \quad [48] \tag{2.4}$$

Where:
ρ_{tap} → Tapped density (percentage of solid state α-alumina bulk density)
ρ_{app} → Apparent density (percentage of solid state α-alumina bulk density)

Table 2.5: Density and Hausner index of α-alumina powders [48]

	ρ_{app} [%]	ρ_{tap} [%]	**H**
Powder F	36.8 ± 3.3	53.8 ± 1.2	1.5 ± 0.1
Powder XF	30.7 ± 1.6	37.8 ± 0.6	1.2 ± 0.1

Several simulations based on the Lubachevsky-Stillinger (LS) algorithm were conducted to process about 2000 spherical particles. The particles had random diameters ranging from 0.1 - 50 μm and were packed inside a cubic periodic box with volume W. The relative density of the jammed configuration was computed using Equation 2.5. According to the study, the average density of both the XF and F particles were 68.4% and 68.9% respectively. The mean number of spheres that are in contact for both the XF and F particles were 4.63 and 5.31 respectively. The simulated jammed configuration with respect to the real arrangement of powder grains is shown in Figure 2.20. Given that powder XF had a larger powder size dispersion than powder F, the packing density can also be seen to be improved in powder XF. The volume fraction determined through LS simulation overestimated the tapped density of both powders; 53.8% ± 1.2% for powder F with an error close to 15% and 37.8% ± 0.6% for powder XF with an error close to 30%. The overestimation is mainly due to the spatial and geometrical filling optimization utilized in the LS method which does not account for realistic parameters such as the mechanical properties of the powder grains, gravity, Van der Waals forces, *etc.*

$$\rho_{LS} = (\sum_{i=1}^{N} V_i)/W \quad [48] \tag{2.5}$$

Where:
ρ_{LS} → Relative density
N → Number of spheres
V_i → Characterized volume of each sphere
W → Cubic periodic box volume

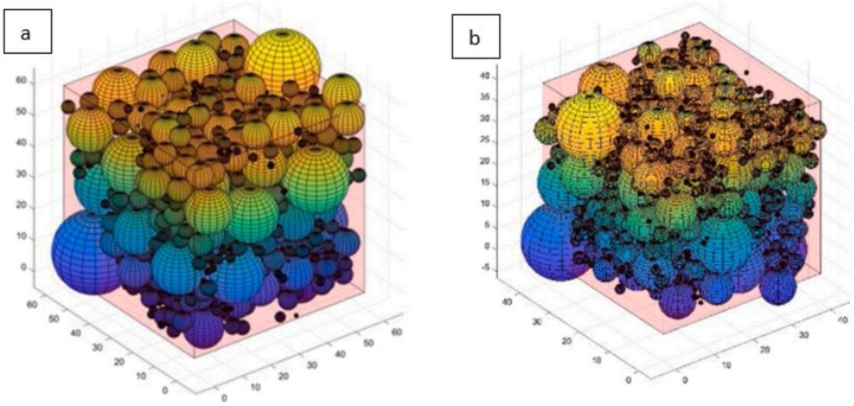

Figure 2.20: Powder packing jammed configuration using LS algorithm: a) Powder F, b) Powder XF [48]

The study also performs a powder packing simulation using the discrete element method (DEM) which analyzes a more realistic packing behavior by interpreting the contact forces and the moment between each particle while considering both the geometrical and mechanical characteristics of the powder. A group of particles with specific particle size distribution (PSD) was generated inside a prismatic box with dimensions of 0.7 × 0.7 × 3.2 mm. These dimensions were chosen to minimize the influence of the walls and to ensure the simulation was conducted within a reasonable time frame. The average density of both the XF and F particles were found to be 61.3% and 60.9% respectively. Figure 2.21 represents the simulated model using the DEM model. The volume fraction determined through the DEM model had the tapped density values of both powders closer to the experimental values compared to the LS simulation (7% error). This error was mainly due to the model not considering the effects of the Van der Waals forces.

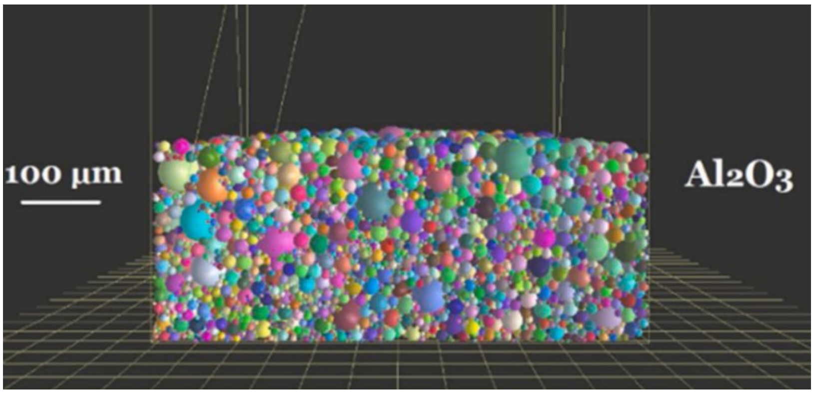

Figure 2.21: Powder packing simulation using DEM [48]

The powders exhibit highly accentuated circularity and shape homogeneity, especially powder F which is essential for facilitating orderly packing and maximizing particle contact points. The flowability of both powders was observed to be poor (Table 2.5). Powder F has a Hausner ratio above 1.2, which is considered the upper limit for free-flowing powders. Powder XF, on the other hand, has a better Hausner ratio, however, the apparent and tapped densities are lower than powder F suggesting an inferior packing density and poor flowability as compaction does not even after tapping. Alumina typically tends to have lower performance than metal powders as they are attributed to lower densities (preventing self-compaction) and smaller particle diameter which promotes aggregation due to Van der Waals interaction and capillarity induced by humidity. This results in the entrapment of air bubbles when depositing a free-flowing powder.

The alumina powders were observed through a scanning electron microscope (SEM) and it revealed that the particles of powder F were almost perfectly spherical in shape with diameters ranging from 1µm to 20-30µm (Figure2.22-A and Figure 2.22-B). Powder F has a minimal internal porosity and from Figure 2.22-B it can be observed that the large particles have fractured surfaces, suggesting that it was formed by sintering the submicron-sized particles. Powder XF, on the other hand, has particles that are smaller and irregular in size (Figure2.22-C and Figure 2.22-D). It primarily consists of submicron-sized particles with fewer larger aggregates.

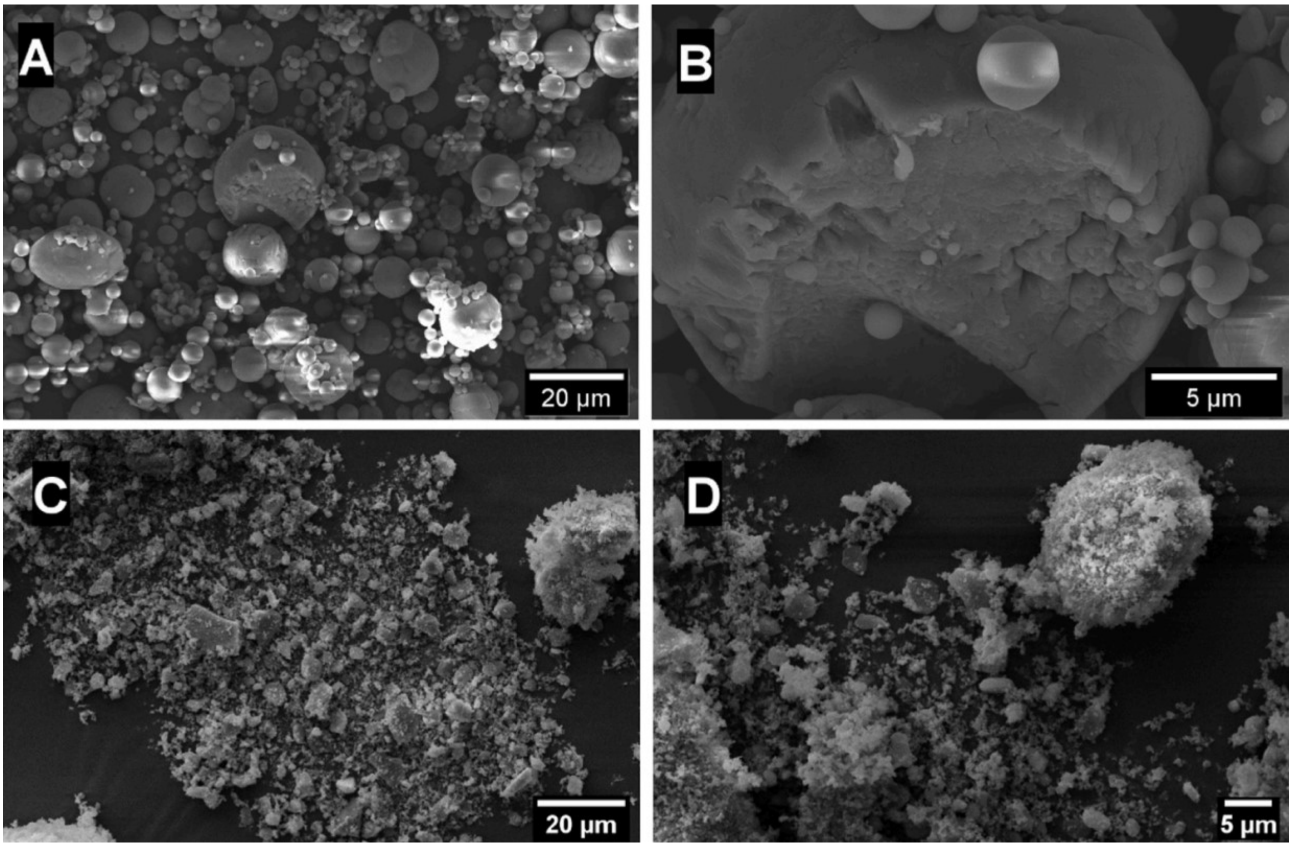

Figure 2.22: SEM images of α-alumina powders: A-B) Powder F, and C-D) Powder XF [48]

In characterizing the green body, the average relative density of the cubes with a binder saturation of 55% was found to be 61.2% and decreased by 1% after debinding, likely due to the evaporation of the binder solvents. The absence of walls in the printing box and the layer-by-layer deposition and spreading of the powder likely contributed to the improved packing. In the parallelepiped samples, the relative density with binder saturation of 55% was superior to those values reported in Table 2.3 for unimodal alumina powders deposited through BJ. This suggests that the geometrical characteristics of the powder, such as particle size, shape, and distribution, play a significant role in improving packing density more than its flowability. A large difference in the green densities can be observed when comparing the components with different binder saturation. This suggests that larger voids are formed during the elimination of the volatile binder component due to the increase in the amount of polymer present in the binder, which as a result leads to a decrease in the final density and less precise geometry. Bending tests were performed on the green samples and it revealed that the flexural strength values ranged between 3 to 10 MPa. The bonding strength provided in this phase is only due to the presence of a cured polymer network. The wide range of results pertaining to stiffness and maximum load can be attributed to the irregular internal structures of the samples which results in the unpredictable formation of defects and cracks during testing.

In characterizing the sintered body, the optimal sintering cycle was determined. The increase in the relative density of cubic samples was measured after thermal treatments (75.4 ± 1.4%). Cycle B with an increased peak temperature and slower heating ramp, proved to be more effective in the sintering process compared to cycle A. The samples were significantly densified as a result of Cycle B (+14%) and caused necking between the particles. However, the study was unable to achieve full density and some open porosity still remained. The bending test performed on the sintered samples suggested a lower final density (61.8 ± 1.2%) compared to the cubic samples, however, it still had a similar densification rate (12%). The shrinkage rates in all directions were about 7%, but the differences from the intended dimensions were negligible. The flexural strength of the samples was comparable to similar-density alumina components produced through BJ. However, it was lower than those obtained from conventional methods or other additive manufacturing techniques. The main reason for the lower mechanical resistance was the presence of pores and defects that accelerated the crack formation. The fracture surface also indicated the presence of anisotropic mechanical behavior which is mainly due to the layer-by-layer printing process. Figure 2.23 shows the SEM images of the fracture surface of the sintered parts from both heat treatment cycles.

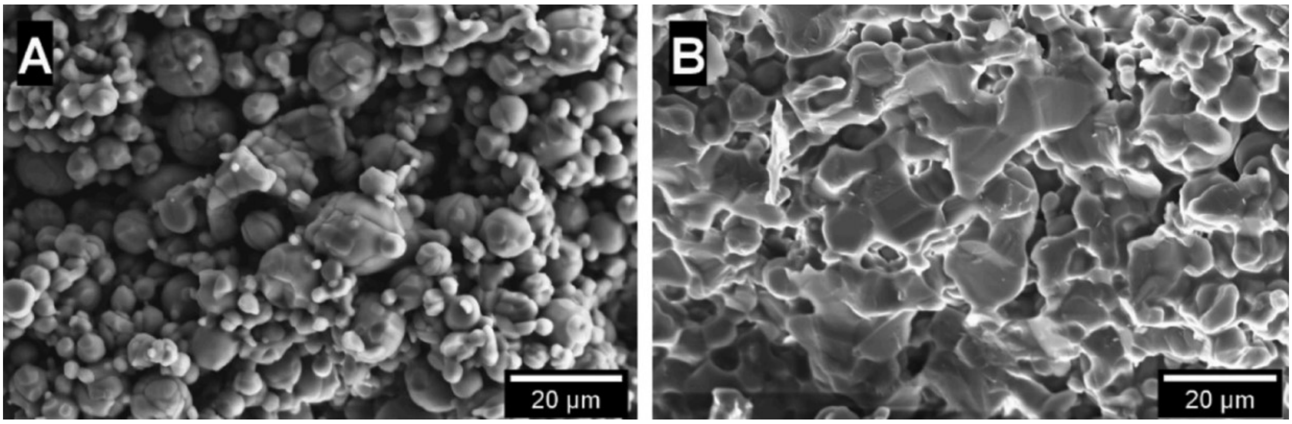

Figure 2.23: SEM images of the fracture surface of sintered parts: A) Cycle A, and B) Cycle B [48]

Overall, the study utilizes a simple printing and post-processing process using BJ. Highly dense green bodies (61.2%) were obtained by optimizing the PSD and later achieved a higher sintered density (75.4%). The study also suggests that an increase in the dimensions of the specimen would result in a decrease in the density. The study can still be further enhanced by improving the densification of the parts.

2.9 Summary

In conclusion, this chapter comprehensively overviewed the background information relevant to the thesis project. The chapter also includes a literature review on the binder jetting of alumina, which is one of the materials that will be tested during the thesis project.

From the literature study (binder jetting of alumina), certain research gaps are yet to be addressed, some of which will be focussed in this thesis project:

- Powder Behavior and Flowability: The report highlights the challenges posed by the low density and reduced average diameter of alumina powder, which affect its flowability and compaction. Additional research is needed to investigate the underlying mechanisms that hinder the flowability of small-sized particles and explore strategies to improve their flow behavior, such as surface treatment, particle coating, or adjusting the powder formulation. Understanding and enhancing powder flowability can help improve the packing density and improve overall printing performance.

- Sintering Optimization: The report identifies the need to optimize the sintering process in order to achieve full densification of the printed components. Further research should focus on developing optimized sintering parameters, exploring alternative sintering techniques (e.g., microwave sintering or spark plasma sintering), and investigating the effect of different heating profiles and dwell times on the sintering behavior and final properties of the components. This research will help overcome the challenges associated with achieving higher densification and reduce the presence of residual porosity in the sintered samples.

- Mechanical Performance: The mechanical strength and performance of the printed and sintered components can be further improved. Research should aim to enhance the bonding strength between particles, reduce the presence of defects and cracks, and optimize the microstructure to achieve higher mechanical properties. Investigating the effect of different processing parameters, such as binder saturation, layer thickness, and printing strategies, on the mechanical performance will provide valuable insights for enhancing the overall structural integrity and reliability of the printed components.

- Advanced Characterization Techniques: Performing microstructural analysis using scanning electron microscopy (SEM) with energy-dispersive X-ray spectroscopy (EDS) can help provide detailed information about the internal structure, pore distribution, and phase composition of the printed and sintered components.

2.10 Research Objectives

Given the literature study done above, this research will focus on the following research objectives:

- Material and Design Optimization: The primary objective of this study is to identify a suitable high-purity ceramic material(s) to replace SS316L in REMA blades. Additionally, the research aims to optimize the existing REMA blade design for manufacturing using binder jetting technology, with a focus on reducing or eliminating the cooling channels present inside the REMA blades. The newly designed blade should also be assessed by performing thermo-mechanical simulations according to the ASML's standards.
- Process Optimization: The secondary objective is to determine the optimal printing and sintering parameters that can result in achieving high density in both green body and sintered body with high accuracy (low shrinkage rate).
- Functional Optimization: The final objective is to achieve highly dense parts (>90%) with Young's modulus and flexural strength that either meet or exceed the properties of SS316L.

CHAPTER 3

MATERIALS AND METHODS

3.1 Materials and Processing

In this research, α-alumina powders (99.9% purity) of four different sizes were used to additively manufacture alumina samples. The alumina powder is spherical and had mean particle sizes of 20 µm (BAK-20, xtra GmbH, Germany), 10 µm (BAK-10, xtra GmbH, Germany), 5 µm (BAK-5, xtra GmbH, Germany), and 2 µm (BAK-2, xtra GmbH, Germany). Table 3.1 and Table 3.2 show the physical characterizations and the chemical composition of these powders respectively. In the initial phase of the research, separate batches of 20 µm and 10 µm were used for printing the alumina samples to test the print quality and density. In the later stages of the research, a trimodal batch consisting of 10 µm, 5 µm, and 2 µm powders were mixed at equal concentrations (33%) using a roller mixer (Assistent RM 5F, Glaswarenfabrik Karl Hecht GmbH & Co. KG, Germany), to understand how the particle sizes affect the green body and sintered body density. Prior to the printing process, the individual powder batches were dried thermally using an oven (Yamato DX412C, Japan) at 200°C for 6 hours, the trimodal batch on the other hand, was dried overnight. The powder was then removed from the oven and manually mixed for approximately 5 minutes using a scoop. Drying the powder is crucial to control the moisture content which adversely affects the flowability, packing density, and sintering properties of these materials. Moisture can cause powder particles to agglomerate or clump, resulting in uneven layer deposition. The dried powder was sieved through a mesh size of 106 µm (140 mesh) to ensure proper distribution of powder. The sieved powder was later stored in the hopper bin which deposits the powder onto the powder bed (Figure 3.2-A). The liquid binder used during the printing process was a standard aqueous-based binder with a density of 1.06 g/cm^3 provided by ExOne (Huntington, PA, US). In order to understand the properties of the additively manufactured alumina samples, conventional alumina samples (Ceramic Partner, 's-Hertogenbosch, Netherlands) manufactured through cold-pressing of dimensions 45 x 4 x 3 mm per ASTM C1161-13 standard were ordered to provide a reference.

Table 3.1: Physical characterization of the alumina powders used

Properties		**BAK-20**	**BAK-10**	**BAK-5**	**BAK-2**
Particle Size (µm)	**D$_{10}$**	13.42	6.19	3.89	0.71
	D$_{50}$	21.52	10.55	5.92	1.08
	D$_{90}$	33.72	16.7	8.82	3.21
Specific Surface Area (m$_2$/g)		0.14	0.17	0.36	1.69
Electrical Conductivity (µS/cm)		6.87	4.05	5.65	6.07
pH		7.62	7.9	7.7	7.53
Moisture (%)		0.03	0.03	0.03	0.05
True Density (g/cm^3)		3.79	3.76	3.74	3.71
Spheroidization (%)		96	98	98	96

Table 3.2: Chemical compositions of the alumina powders used

Powder	**Al_2O_3 (%)**	**SiO_2 (ppm)**	**Fe_2O_3 (ppm)**	**Na_2O (ppm)**	**Loss (%)**
BAK-20	99.92	150	60	140	0.04
BAK-10	99.94	20	40	60	0.04
BAK-5	99.89	430	140	10	0.05
BAK-2	99.87	430	140	90	0.06

The PSD of all the alumina powders was determined using a laser diffraction particle size analyzer (Microtrac Bluewave S3500 SI, Microtrac Inc., USA). The powder sample was mixed with distilled water to form a suspension. A pipette was used to insert a small amount (a few mL) of the suspension into the sample bay of the analyzer. The analyzer performs the PSD measurements via laser scattering and produces the results.

3.2 Fabrication

The alumina parts were fabricated using a binder jetting printer (BJP), ExOne - Innovent Plus (Huntington, PA, US). The ExOne printer had a build envelope of 65 x 65 x 160 mm and the printhead consisted of 256 nozzles. Figure 3.1 shows the BJP used for printing the alumina samples. The ExOne printer incorporates a hopper system that dispenses powder using ultrasonic vibration directly onto the powder bed (Figure 3.2-A). It is important to note that the powder bed is heated (approximately 65°C). This is done to ensure effective binding and improve the flow characteristics of the binder, making it easier to distribute and infiltrate the powder evenly. A heated powder bed also accelerates the binder curing process in order to maintain structural integrity and prevent distortion during the printing process.

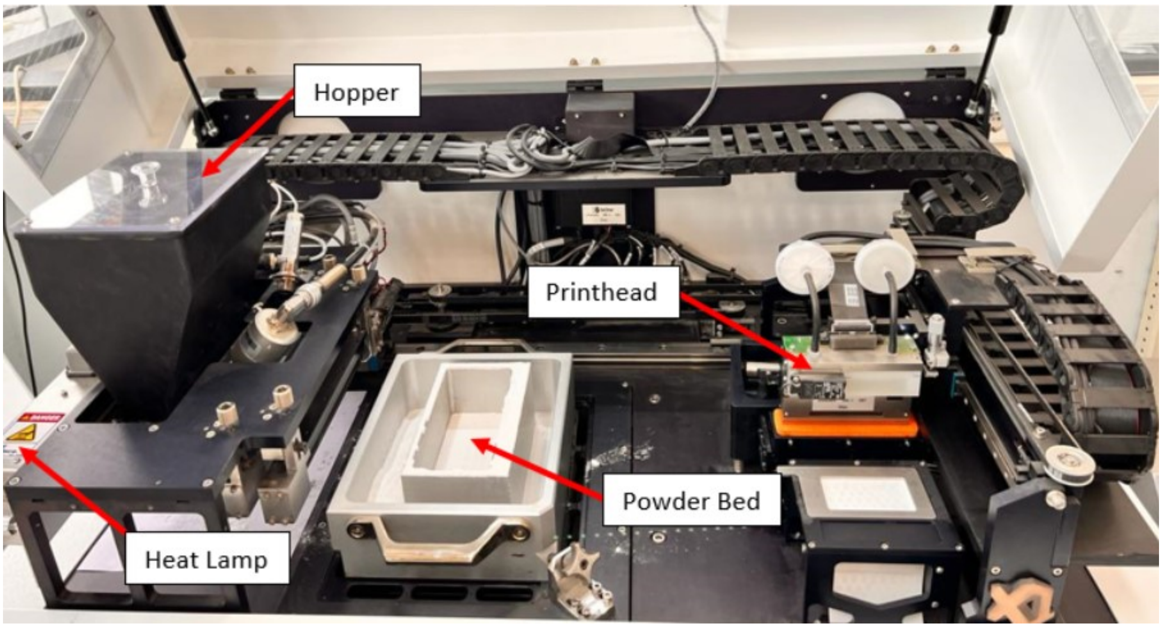

Figure 3.1: ExOne Innovent Plus BJP

The hopper hovers above the powder bed and deposits a thin layer of powder which is flattened using two rollers; rough roller and soft roller (Figure 3.2-B). During printing, the printhead selectively deposits the binder onto the powder bed in the shape of the desired part (Figure 3.2-C). A heat lamp is radiated over the powder bed to initiate the partial curing of the binder (Figure 3.2-E). The powder bed lowers to allow a new powder layer and binder to be deposited. This process is repeated for several layers (based on the part shape and layer thickness). Upon completion of the printing process, the powder bed (along with the fabricated parts) is removed from the printer and placed into an oven where the binder is fully cured at a temperature of 200°C for 6 hours in air, per the recommendations provided by the binder manufacturer (ExOne). The green parts (cured parts) are removed from the powder bed and prepared for further post-processing steps. Figure 3.2 shows the steps involved in BJP.

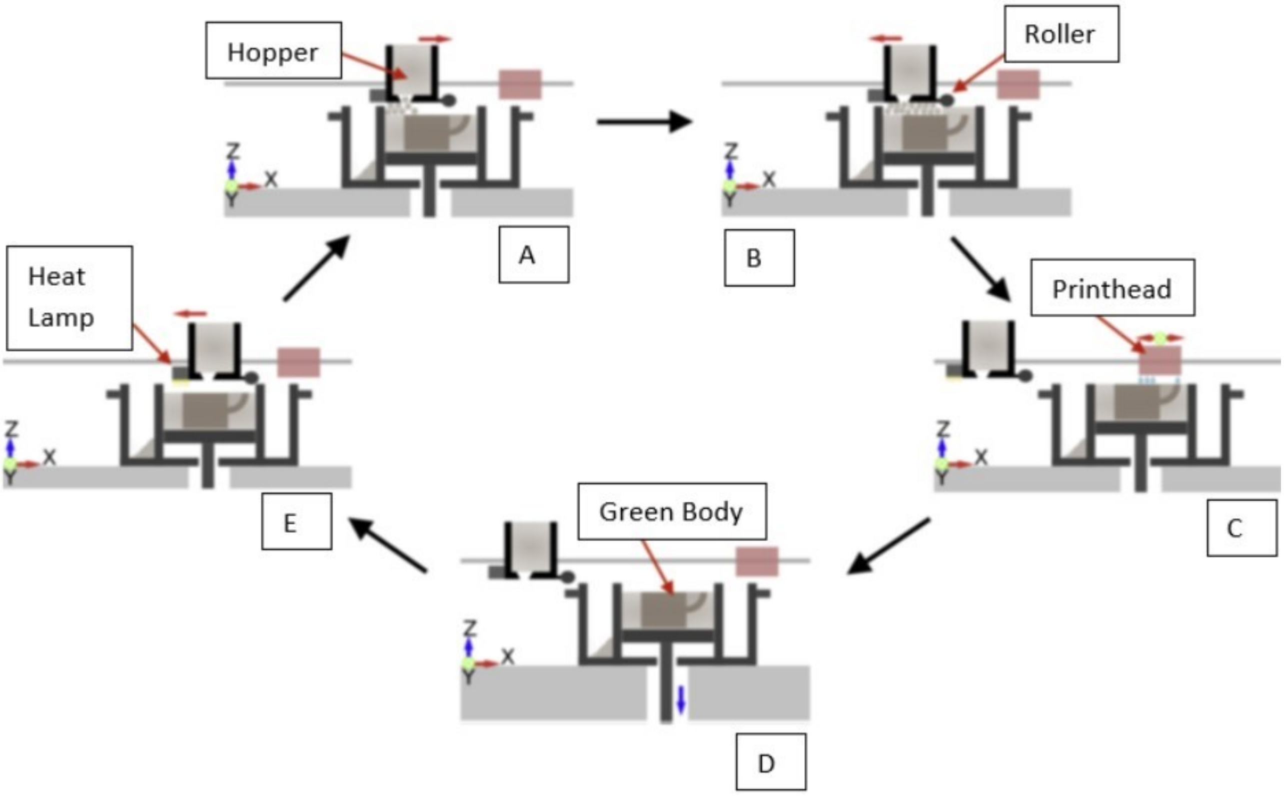

Figure 3.2: A-E) Schematics of BJP [33]

Prior to initializing the print job, the manufacturer (ExOne) recommends performing a Myers test in order to calibrate the rollers to the powder bed. This calibration needs to be performed every time the layer thickness is changed. A thumb rule provided by the manufacturer was that layer thickness is twice the average particle size. For example, for the BAK 10 powder, the layer thickness used was 20 µm. By changing the layer thickness, the binder droplet spacing also changes (increases in the case of BAK-10) to accommodate the selected binder saturation. To perform the Myers test, 15-20 powder level recoats are done on the job box until an acceptable powder bed has been achieved. Then, a normal recoat is done such that the rollers are centered right in the middle of the job and then the recoat is stopped. The powder bed was lowered at least by 5 mm (z-axis) and then the recoater (hopper system) was retracted. The powder bed was inspected to see if there were two piles of powder present; one in front of the smooth roller and the other in front of the rough roller. Depending on how clearly visible the piles are the printing parameters like recoat speed and ultrasonic intensity need to be adjusted to control the amount of powder being dispensed. Figure 3.3 shows an acceptable Myers test that was performed for the BAK-10 powder.

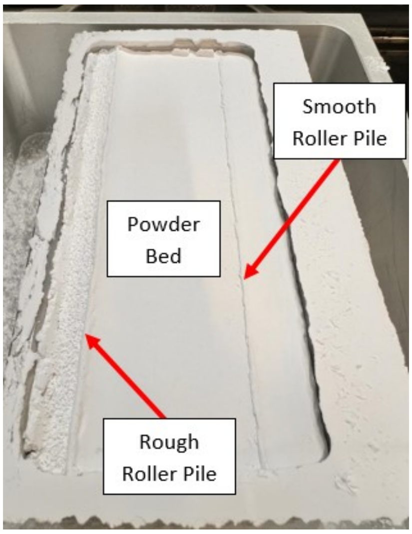

Figure 3.3: Acceptable Myers Test for BAK-10 powder

3.3 Density Characterization

Several rectangular samples with dimensions of 45 X 4 X 3 mm were printed per the ASTM C1161-13 standard to perform the density and mechanical tests. The relative densities (Equation 3.1) of the green bodies were measured using the geometric method whereas the relative densities of the sintered part were measured using both geometric and buoyancy methods. This is because, the buoyancy method based on Archimedes' principle (ASTM B962, 2008) is highly inaccurate due to the presence of the cured binder in the green body which dissolves upon being submerged in water (or any other fluid) and it comprises the integrity of the green body. This method yields a higher density value than the true density of the material especially due to the absorption of the fluid (water) given that the printed part contains open porosities which when infiltrated with water, produce a large overestimation (up to 30%) of the sintered densities. The geometric method is a more suitable and accurate approach for measuring the density of objects with complex shapes, irregular surfaces, or porous structures. In this method, the density is calculated by measuring the dimensions (length, width, and height) of the object and determining its mass. The mass is measured using a balance (321LX, Precisa Gravimetrics AG, Dietikon, Switzerland) with a resolution of 0.001 g. The dimensions are measured using a digital caliper (Mitutoyo CD-15APX) with a 0.01 mm resolution. The measurements are replicated five times and then averaged to ensure accuracy. While acknowledging the buoyancy method's suboptimal characteristics, it was nonetheless deemed pertinent for assessing the disparity in relative density between the two methodologies, given its prevalent usage in numerous scholarly works.

$$\rho_{relative} = \frac{\rho_{experimental}}{\rho_{theoretical}} * 100\% \tag{3.1}$$

Where:
ρ_{relative} → Relative Density (%)
$\rho_{\text{experimental}}$ → Density found using geometric method (g/cm^3)
$\rho_{\text{theoretical}}$ → Theoretical Density (g/cm^3) → ρ_{Alumina} = 3.95 g/cm^3

3.4 Post-Processing

The green body is placed inside the furnace (LHTG 200-300/22-2G, Carbolite Gero GmbH & Co. KG, Germany). The furnace incorporates an argon atmosphere where the debinding and sintering of the green body occurs. The alumina part initially goes through a debinding process at 600°C with a heat rate of 2°C min^{-1} for three hours and 1000°C with a heat rate of 3°C min^{-1} for two hours. The samples are then subjected to sintering at 1650°C with a holding time of 24 hours at a constant heat rate of 5°C min^{-1}.

3.5 Mechanical Characterization

The Young's modulus and flexural strength of the rectangular samples were measured using a three-point bending in a universal tensile testing machine (E20000, Instron, USA) per ASTM C1161-13 standard for testing the flexural strength and Young's modulus of the ceramic sample. In the three-point bending test, a small portion of the sample is exposed to the maximum stress. The sample is carefully loaded between cylindrical bearing edges. These bearing edges are used to support the test sample and load application. It is important to note that the sample should have an equal amount of overhang beyond the outer bearings and be centered directly below the axis of the applied load. The tensile testing machine is coupled with an extensometer with a gauge length of 50 mm to measure the axial displacement as seen in Figure 3.4. The load must be applied slowly to the sample.

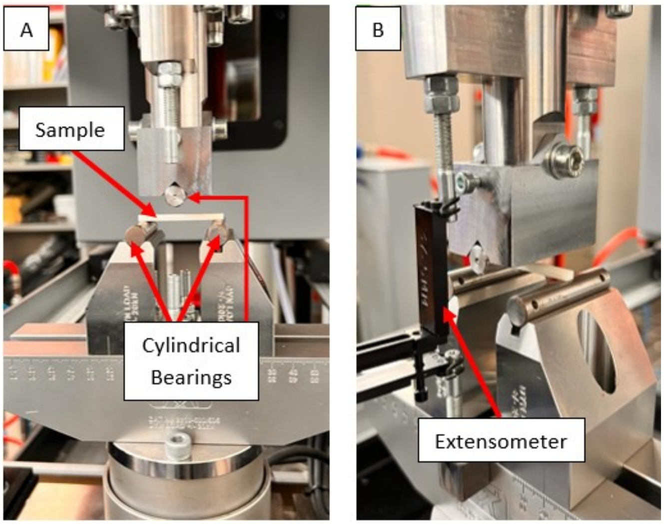

Figure 3.4: Experimental setup for the three-point bending test

The Young's modulus of the samples can be calculated from the data provided by the bending tests. The three-point bending test provides data about the applied load/force (in kN) on the sample and the strain experienced by the extensometer until the sample breaks. Through the strain, the displacement experienced by the extensometer can be determined. With the force and displacement data, a scatter plot was made for all the samples. For the three-point bending test (Figure 3.5, the deflection of a rectangular beam is determined using Equation 3.2. The slope (m) of the linear component in the graph was taken to calculate Young's modulus of the sample and can be represented using Equation 3.3. Rearranging Equation 3.3 to determine the Young's modulus results in Equation 3.4. The moment of inertia (I) of the samples can be determined using Equation 3.5 wherein, the sample is assumed to be a rectangular beam. Combining Equation 3.4 and Equation 3.5 results in Equation 3.6, through which the Young's modulus of the sample can be calculated.

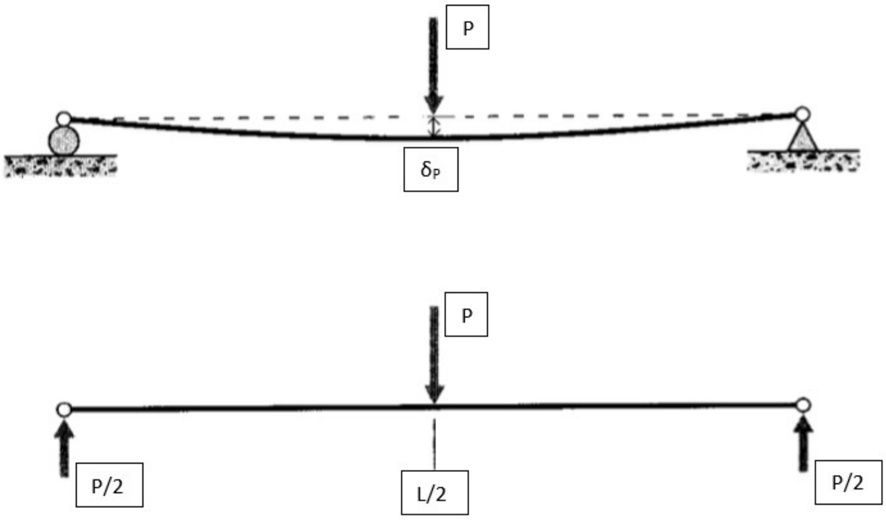

Figure 3.5: Three-point bending

$$\delta_P = \frac{PL^3}{48EI} \quad [67] \tag{3.2}$$

Where:
δP → Deflection of the rectangular beam
P → Force (or load) acting on the rectangular beam
L → Length of the rectangular beam
E → Young's modulus of the rectangular beam
I → Moment of inertial of the rectangular beam

If the applied force (P) is plotted against central displacement (δP), a straight line is obtained; provided it remains within the elastic limit of the material (i.e. the beam returns to its original shape after deflection). The gradient of this line is given as:

$$m = \frac{48EI}{L^3} \quad [67] \tag{3.3}$$

Where:
m → Gradient of the linear component (from the graph)

$$E = \frac{mL^3}{48EI} \tag{3.4}$$

$$I = \frac{bh^3}{12} \tag{3.5}$$

Where:
b → Width of the rectangular sample
h → Height (or depth) of the rectangular sample

$$E = \frac{mL^3}{4bh^3} \tag{3.6}$$

3.6 Microstructural Characterization

3.6.1 Sample Preparation

The sintered samples were cut into smaller sections using a water-lubricated rotating diamond cutting wheel machine (Accutom 100, Struers, USA) with low force, rotation speed of 3000 rpm, and a travel speed of 0.050 mm/s. The samples are then cold-mounted with epoxy resin (ClaroCit, Struers, Denmark). This specimen is ground using SiC abrasive paper with various grit sizes; P320 (two minutes), P800 (two minutes), P1200 (two minutes), P2000 (two minutes), and P4000 (four minutes). The ground samples are then polished using a diamond paste 3µm for four minutes and 1µm for four minutes. The polished samples are immersed in a beaker filled with isopropanol and then cleaned using an ultrasonic cleaner. After these procedures, the samples (hereby referenced as specimens) are made conductive by coating a thin layer of carbon via sputter deposition using an automatic carbon sputter coater (JEC-530, Jeol, Japan).

3.6.2 Material Characterization

The cross-sectional images of the specimen were taken using an SEM (JSM-IT100, Jeol, Japan) and were used for microstructural analysis. EDS was also performed on the specimen using the same equipment to analyze the elemental composition of the specimen. In order to evaluate the phase composition of the specimen, an X-ray diffractometer (XRD) analysis was performed using a Bruker D8 Advance diffractometer with Cu Kαradiation, V12 divergence slit, scatter screen height 5 mm, 45 kV voltage, 40 mA current, and scan angles ranging from 10° to 110° with 0.03° steps.

CHAPTER 4

RESULTS AND DISCUSSION

4.1 Material Selection Process

The materials were selected using the ANSYS CES Granta EduPack software, where various ASHBY plots were plotted. The existing REMA blades are made of stainless steel 316L. The properties of the 316L were considered as a baseline to narrow down materials with better properties. These properties are listed in Table 4.1. Minimizing the density and CTE while maximizing the remaining properties was key in determining the new set of materials. To further narrow down the list of materials, only ceramic materials were selected to fit the purpose of this project. This led to a total of 339 ceramic materials which also included ceramic composites.

Table 4.1: Stainless steel 316L properties

Properties [units]	**Value**
Density [kg/m^3]	8000
Young's Modulus [GPa]	193
Specific Stiffness [MN.m/kg]	23.8 - 25.8
Flexural Strength [MPa]	170 - 310
Fracture Toughness [MPa.m$^{0.5}$]	4.3
Thermal Conductivity [W/m.°C]	16
Specific Heat [J/kg.°C]	500
CTE [µstrain/°C]	15.5

The first ASHBY plot considered was Young's modulus vs. density (Figure 4.1). The objective was to consider materials with lower density than stainless steel 316L and higher Young's modulus.

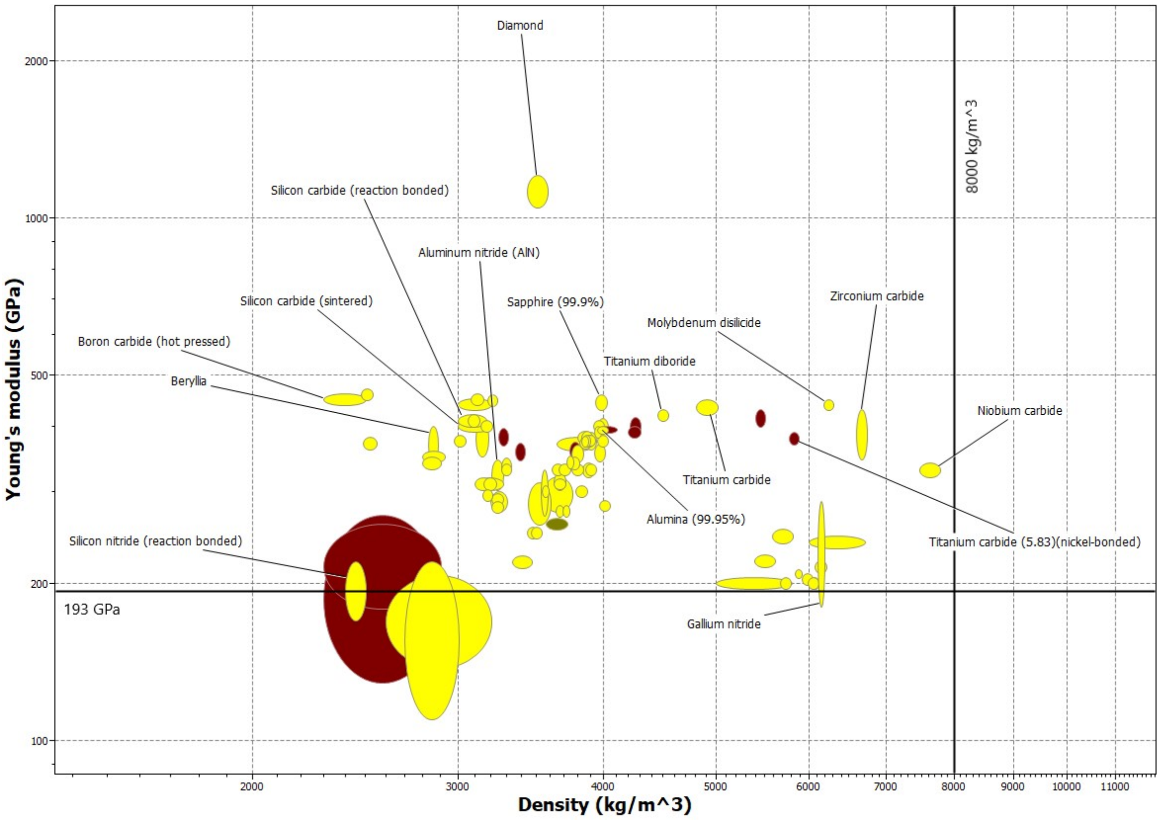

Figure 4.1: Young's Modulus vs Density - ASHBY plot

The second ASHBY plot considered was thermal conductivity vs coefficient of thermal expansion (Figure 4.2). The objective here was to consider materials that had higher thermal conductivity and thermal expansion than stainless steel 316L.

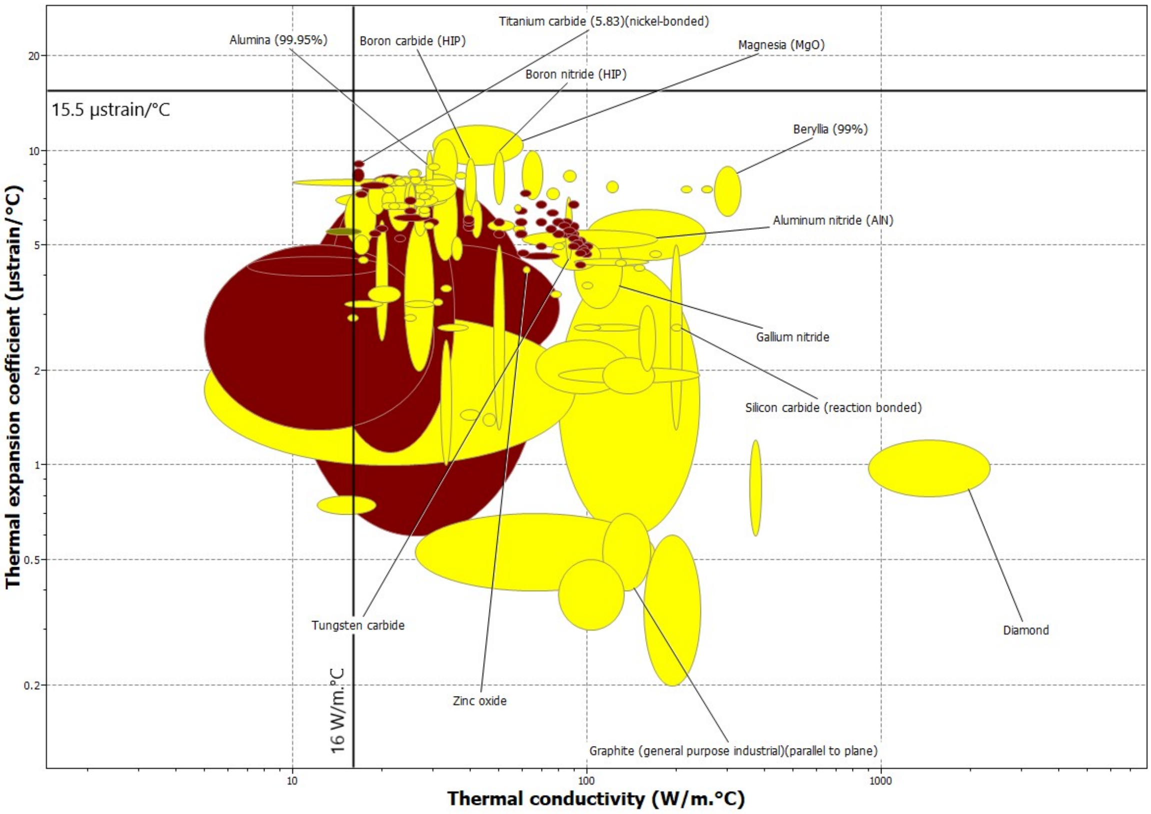

Figure 4.2: Thermal Conductivity vs Coefficient of Thermal Expansion - ASHBY plot

The third ASHBY plot considered was fracture toughness vs. Young's modulus (Figure 4.3). The objective here was to consider materials that had higher fracture toughness and Young's modulus than stainless steel 316L.

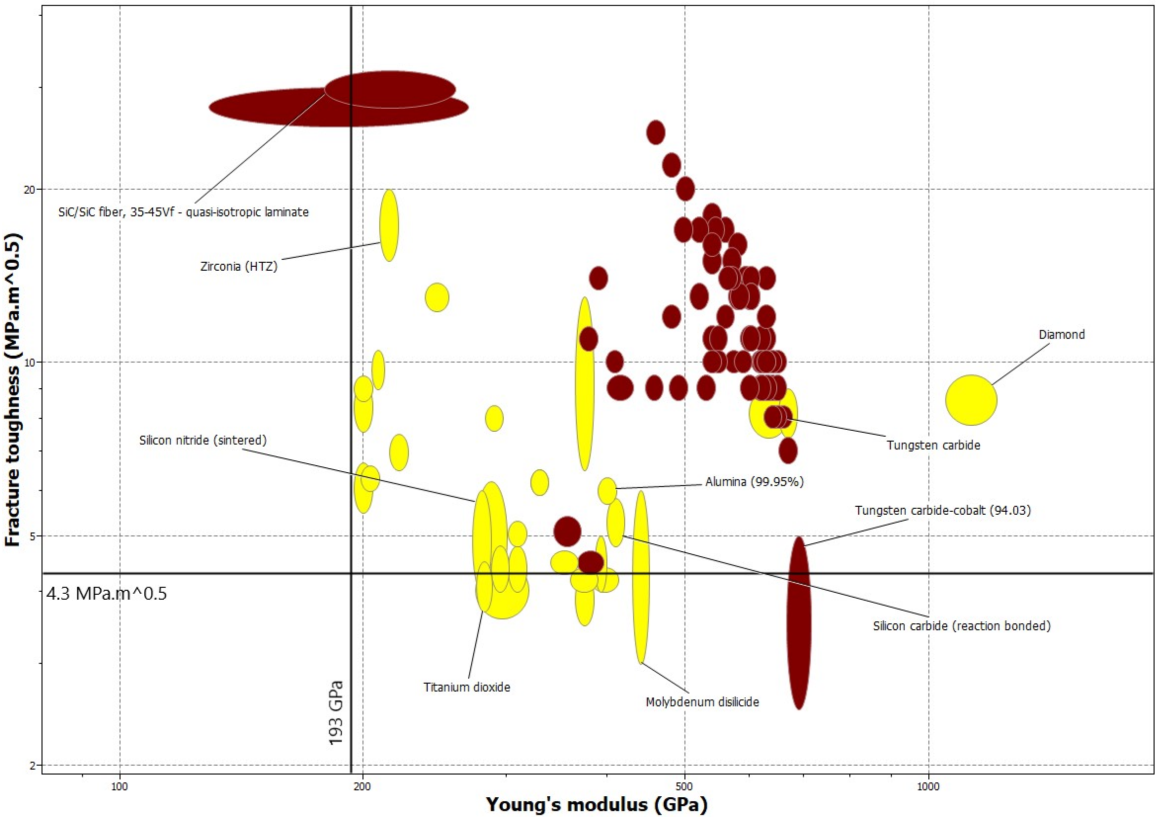

Figure 4.3: Fracture Toughness vs Young's Modulus - ASHBY plot

The final ASHBY plot was considered was specific heat capacity vs. thermal conductivity (Figure 4.4). The objective here was to consider materials that had higher specific heat capacity and thermal conductivity than stainless steel 316L.

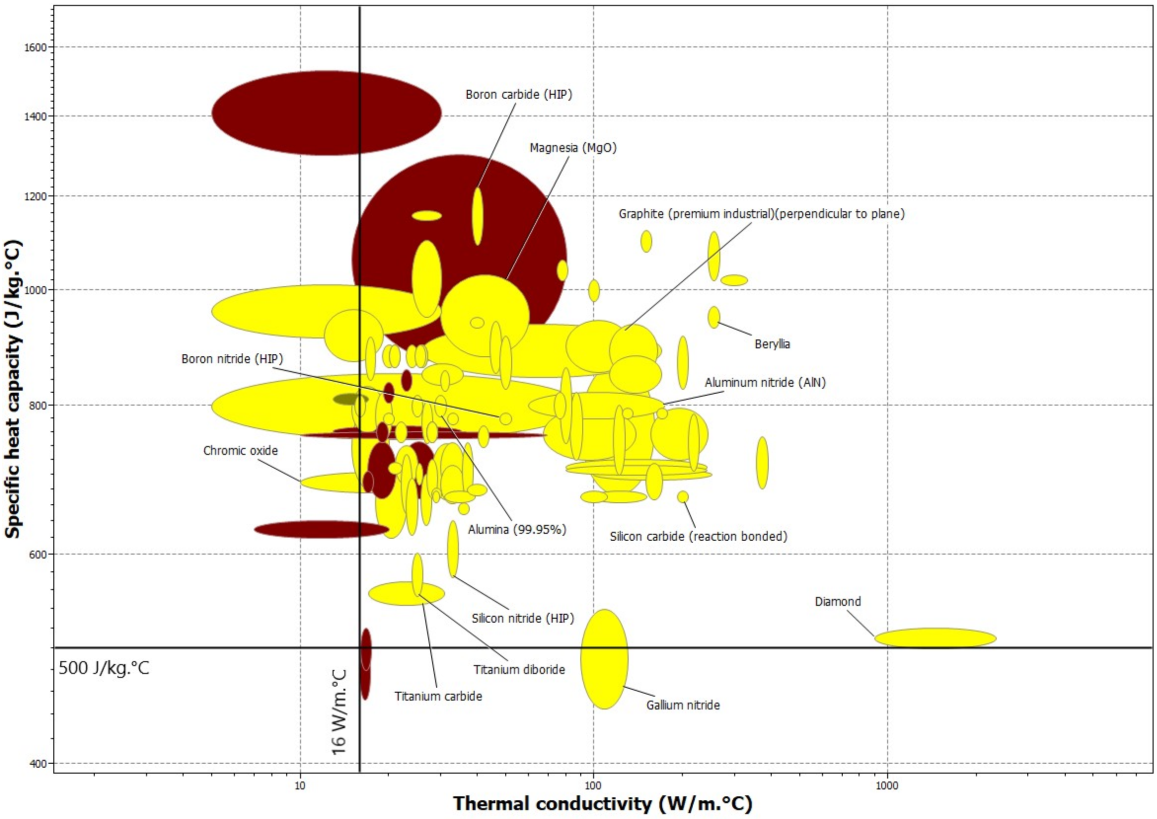

Figure 4.4: Specific Heat Capacity vs Thermal Conductivity - ASHBY plot

Finally, the materials that intersected with all the graphs were taken into consideration. The materials that barely didn't meet the requirements were also considered to ensure a good estimation of the materials selected. Amongst these materials, three materials were carefully selected based on their properties as well as their current application in the ASML machines. The selected materials were: silicon carbide (reaction bonded), also known as, siliconized silicon carbide (SiSiC), aluminum nitride (highest purity available), and alumina (highest purity available).

4.1.1 Silicon Carbide (reaction bonded)

Silicon carbide (reaction bonded), more commonly known as siliconized silicon carbide (SiSiC) is a type of ceramic where silicon carbide (SiC) is combined with silicon (Si) through the process of infiltration. In the process, molten Si is infiltrated into porous SiC preform which forms a SiC matrix with embedded Si particles [21]. SiSiC has many desirable properties which is why they have a wide range of applications. They have high strength and will not deform or fail when exposed to high stresses and loads. They have excellent thermal conductivity, resistance to corrosion, high electrical conductivity, low CTE, low density, and high wear resistance. They are typically used in kiln furniture, semiconductor processing (like wafer carriers), aerospace components, medical implants, armors *etc.*

Table 4.2: Siliconized Silicon Carbide (SiSiC) properties

Properties [units]	**Value**
Density [kg/m^3]	3000 - 3170
Young's Modulus [GPa]	400 - 420
Specific Stiffness [MN.m/kg]	128 - 138
Flexural Strength [MPa]	354 - 391
Fracture Toughness [MPa.m$^{0.5}$]	4.8 - 5.8
Thermal Conductivity [W/m.°C]	192 - 208
Specific Heat [J/kg.°C]	663 - 677
CTE [µstrain/°C]	2.7 - 2.8

4.1.2 Aluminum Nitride

Aluminum nitride (AlN) is one of the most widely used nitride-based ceramic materials. AlN is produced when alumina reacts with nitrogen gas (N_2) through the nitridation process at high temperatures and pressures [5]. AlN is a high-performance material with excellent thermal conductivity, high strength, low density, low CTE (almost close to Silicon) good electrical insulation, good thermal shock resistance, and high corrosion resistance. Table 4.3 shows various properties of aluminum nitride which was considered for the material selection process. Although the fracture toughness of AlN is slightly lower than stainless steel 316L, the other properties of AlN are much superior comparatively. Similar to alumina, AlN also has a wide range of applications due to its material properties. AlN is used as substrate material for electronics, heat sinks, *etc.* They are also used in semiconductor processing, aerospace components, medical implants, cutting tools, refractories, and many more [28].

Table 4.3: Aluminum nitride properties

Properties [units]	**Value**
Density [kg/m^3]	3270 - 3300
Young's Modulus [GPa]	323 - 348
Specific Stiffness [MN.m/kg]	97.8 - 106
Flexural Strength [MPa]	232 - 290
Fracture Toughness [MPa.m$^{0.5}$]	2.5 - 3.1
Thermal Conductivity [W/m.°C]	163 - 177
Specific Heat [J/kg.°C]	781 - 795
CTE [µstrain/°C]	4.6 - 4.8

4.1.3 Alumina

Aluminum oxide (Al_2O_3), more commonly known as Alumina is one of the most widely used oxide-based ceramic materials. Alumina is produced through bauxite via the Bayer process [8]. High-purity alumina is a versatile material with a wide range of applications including electronic components, medical implants, aerospace components, refractories, cutting tools, *etc.* Their wide range of applications is mainly due to their exceptional material properties. They are specifically known for their excellent wear and corrosion resistance, high thermal conductivity, high mechanical strength, and low density amongst other positives [3]. Table 4.4 shows various properties of high-purity alumina (99.9%) which was considered for the material selection process.

Table 4.4: Alumina properties

Properties [units]	**Value**
Density [kg/m^3]	3860 - 3930
Young's Modulus [GPa]	367 - 384
Specific Stiffness [MN.m/kg]	94.1 - 98.8
Flexural Strength [MPa]	264 - 312
Fracture Toughness [MPa.m$^{0.5}$]	5.7 - 6.3
Thermal Conductivity [W/m.°C]	28 - 35
Specific Heat [J/kg.°C]	668 - 742
CTE [µstrain/°C]	7.8 - 8.1

This research will exclusively concentrate on alumina due to its abundant availability and cost-effectiveness. Furthermore, alumina has been chosen for its comparatively inferior properties compared to other materials, rendering it a representative worst-case scenario for ASML, particularly in the context of REMA blade fabrication from high-purity alumina.

4.2 Design Optimization

[See attached section for more information]

[ASML proprietary information]

4.3 Thermo-Mechanical Simulations

[See attached section for more information]

[ASML proprietary information]

4.4 Characterization of Conventional Alumina Sample

The conventional alumina sample is considered as a reference material to compare with the binder jetted alumina samples. This sample was fabricated by Ceramic Partner using high-purity (99.7%) α-alumina material which is cold-pressed and then subjected to hot-isostatic pressing (HIP) at 1650°C.

Table 4.5 and Table 4.6 show the calculated relative density of the conventional sample using both the geometric and buoyancy methods respectively.

Table 4.5: Relative density of the conventional sample using geometric method

Sample	**L (mm)**	**W (mm)**	**D (mm)**	**Volume (cm^3)**	**Mass (g)**	**Density (g/cm^3)**	**Relative Density (%)**
Conventional Sample	45.1	4.0	3.0	0.5	2.1	3.9	98.5

Table 4.6: Relative density of the conventional sample using buoyancy method

Sample	**Mass (in air) (g)**	**Mass (in water) (g)**	**Density (g/cm^3)**	**Relative Density (%)**
Conventional Sample	2.0	1.5	3.9	99.0

From the above tables it is evident that the conventional samples have high densification (geometric: 98.5% and buoyancy: 99.0%). The high density also suggests a good fusion of alumina particles. Figure 4.5 shows the SEM images of the cross-sectional surface for the conventional sample which shows the clear presence of pores (highlighted in red circles). The HIP process removes most of the pores and moisture internally thus resulting in higher bulk densities and lower porosities [2]. The presence of these porosities as seen in Figure 4.5 could be directly influenced by the particle size of the alumina used by Ceramic Partners. The smaller and broader particle size distribution typically produces parts with lower porosity and higher bulk density when compared to larger particles [2].

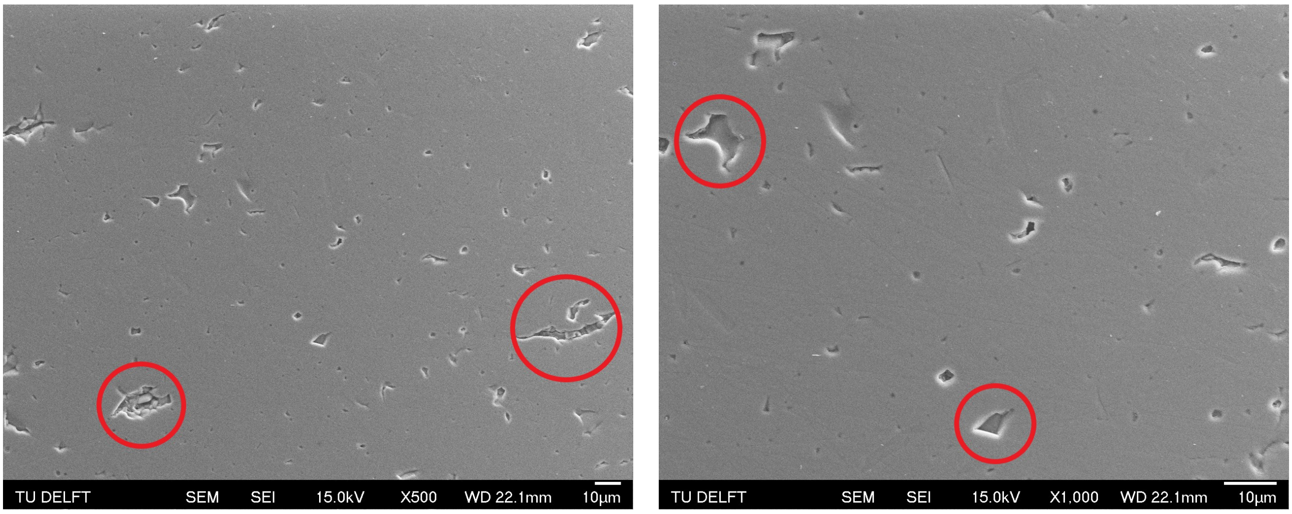

(a) (b)

Figure 4.5: SEM images of the cross-section surface for conventional alumina samples: (a) Overview of the cross-sectional surface, (b) Magnification of the cross-sectional surface

The high density can also be reflected by the part having higher mechanical properties. Figure 4.6 shows the force vs the extensometer displacement determined for the nine conventional samples obtained experimentally through the three-point bending test. The average load at which the conventional samples break is approximately 235 N. The linear component (before the sample breaks) is extrapolated and the gradient of the linear component is determined. The average gradient is determined to be approximately 2307 N/mm which is later used to calculate the Young's modulus values for all the conventional samples using Equation 3.6.

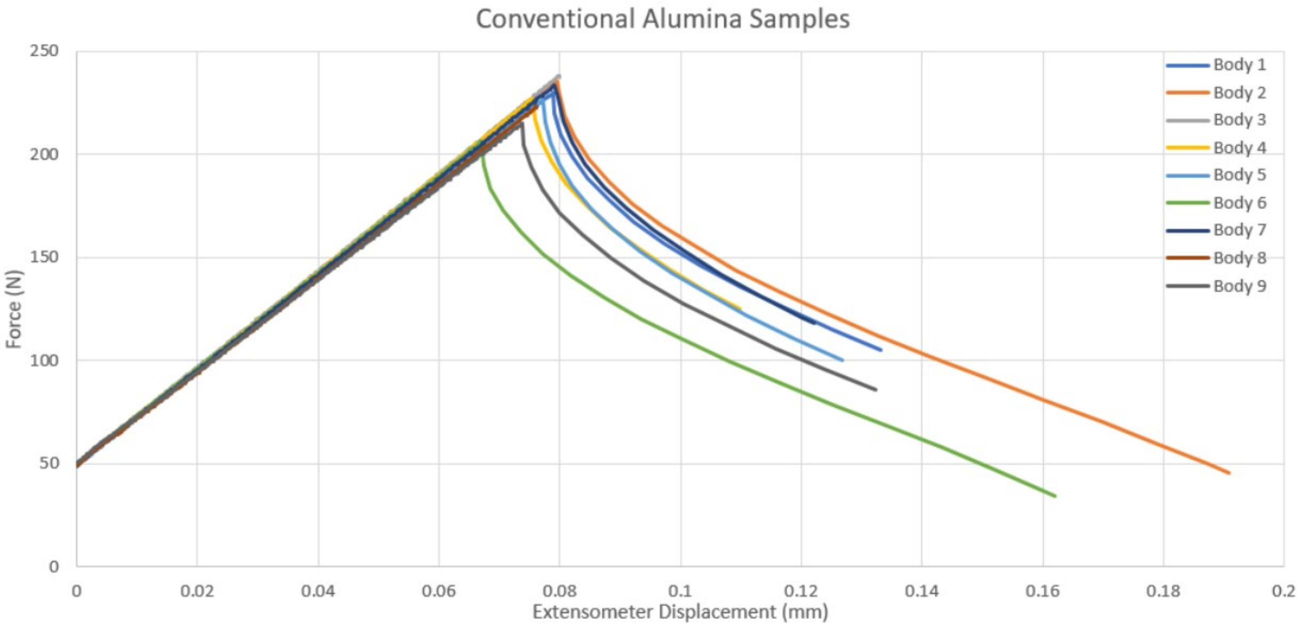

Figure 4.6: Experimental Young's modulus for conventional alumina samples

Table 4.7 shows the average values of Young's modulus and flexural strength for the conventional sample. Young's modulus is determined to be approximately 371 GPa while the flexural strength is 389 MPa. The Young's modulus value obtained is within the range seen in Table 4.4 whereas the flexural strength is higher suggesting a high structural integrity of the conventional sample.

Table 4.7: Young's modulus and flexural stress of conventional alumina samples

Sample	**Gradient (m) (N/mm)**	**Young's Modulus (GPa)**	**Flexural Strength (MPa)**
Average	2307.4 ± 39.6	370.8 ± 9.0	388.8 ± 16.8

The density, microstructural analysis, and mechanical testing results of the conventional samples will compared to the binder jetted alumina samples; UNI-20, UNI-10, TRI-90, and TRI-70.

4.5 Binder Jet Printed Alumina: Material Specific Effect

4.5.1 Effect of Particle Size on Green Body Density

The PSD of BAK-20, BAK-10, BAK-5, and BAK-2 powders are plotted in a frequency vs particle size graph as presented in Figure 4.7. These powders mostly exhibited an unimodal mode with the BAK-20 having a mean PSD of 22 µm, the BAK-10 having a mean PSD of 12 µm, and the BAK-5 having a mean PSD of 7.8 µm. The BAK-2 on the other hand shows two different peaks, one at 5.5 µm and one at 80.7 µm. This could primarily be due to the agglomeration of particles while forming the suspension for the PSD test.

The packing efficiency can be enhanced by using smaller particles as they can occupy the voids between each other during the printing process which yields a higher green body density as it culminates in a more compact powder layer. Finer particles also have a larger surface area when compared to coarser particles [2] which suggests there is an increase in contact surface area between these finer particles, which facilitates higher densification in the green body and during the sintering process [17]. In this research, a 20 µm was initially used to print the rectangular part (UNI-20), which had a lower densification. Therefore, the particle size was decreased by half, to 10 µm (UNI-10) which resulted in a much higher densification. Finally, a trimodal batch (TRI-90 and

TRI-70) was used and yielded significantly higher densification than the unimodal powders. This is due to the smaller particles occupying the voids between the bigger particles thus increasing the green body densification and the compactness of the powder bed.These observations can be seen in Table 4.9

During the print jobs, it was observed that the larger the powder size the better the flowability of the powder which is contrary to what is generally the case. This may be due to the ultrasonic hopper in the BJP. The vibrations caused by the ultrasonic hopper tend to form clumps or agglomerates because of their higher surface area. Larger particles on the other hand have lesser chances of forming clumps or agglomerates which in turn suggests an improved powder flowability. The influence of particle size can be ranked by ordering the impact of powder flowability in an ultrasonic hopper-based BJP. Such ranking yields: BAK-20 > BAK-10 > BAK-5 > BAK-2. The smaller particles are also more susceptible to van der Waals forces and electrostatic forces which inherently help the particles to form clumps and agglomerates [48]. This also makes it very difficult to sieve the smaller particles.

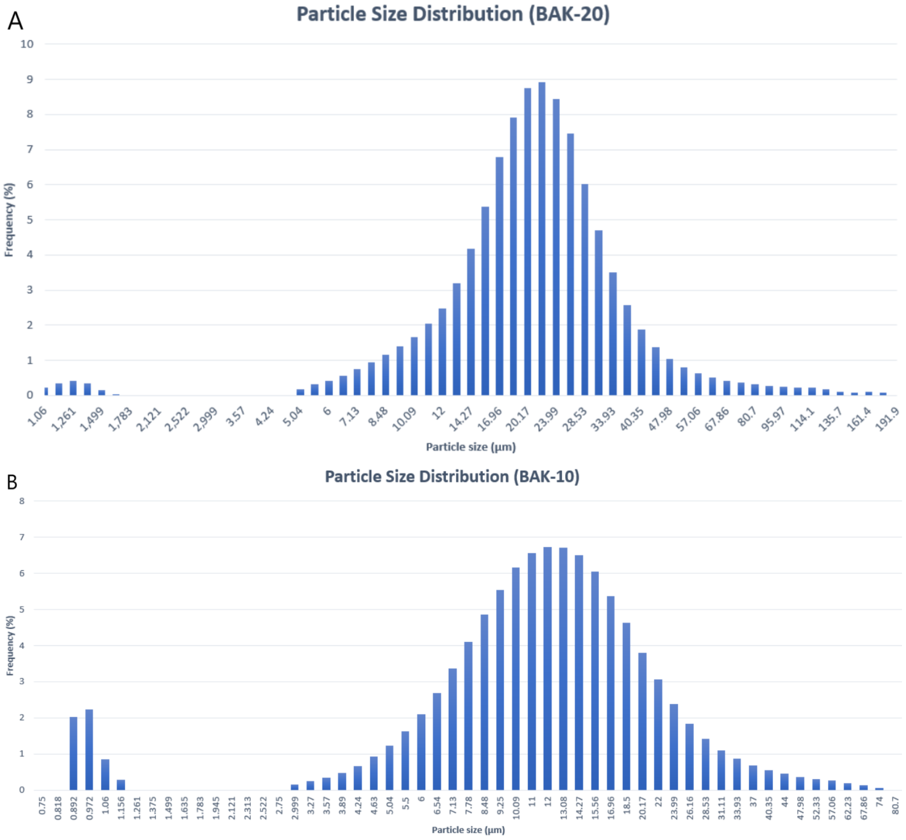

Figure 4.7: PSD of A) BAK-20, B) BAK-10, C) BAK-5, and D) BAK-2

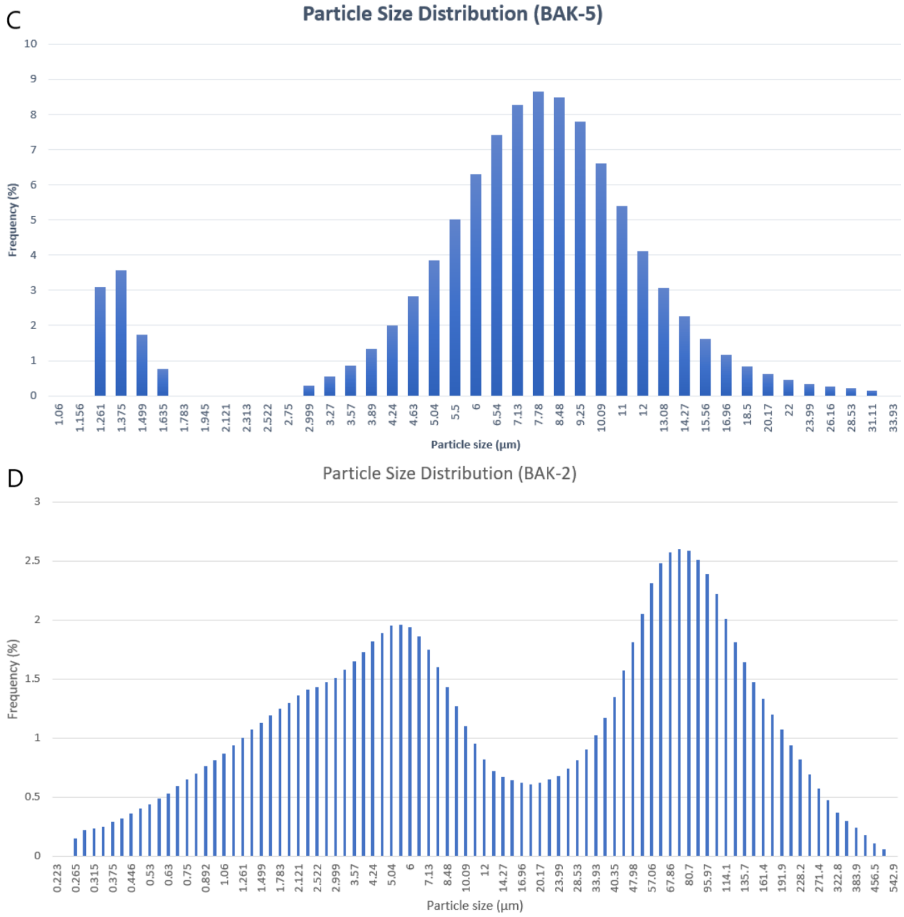

Figure 4.7: PSD of A) BAK-20, B) BAK-10, C) BAK-5, and D) BAK-2, cont.

4.6 Binder Jet Printed Alumina: Process Specific Effects

4.6.1 Effect of Printing Parameters on Green Body Density

The green body densities play a crucial role in determining the quality and integrity of binder jetted components. Higher green densities lead to reduced part shrinkage and can help achieve superior sintering densities. The green body density is predominantly influenced by the flowability of the powder, a characteristic that is, in turn, contingent upon the particle shape [33]. In this research, spherical alumina particles are used as they are considered optimal for binder jetting processes due to their superior flowability, reduced interparticle friction, and excellent packing efficiency. The green body densities of all the samples were determined using Equation 3.1, this is shown in Table 4.9.

Various parameters were employed for the fabrication of the alumina parts from each powder composition, and the parameter set yielding an intact green body part and highest density has been selected for detailed explication in this research. Table 4.8 shows this parameter set.

Table 4.8: Printing parameters used for the alumina samples

Samples	Binder Saturation (%)	Binder Set Time (s)	Drying Time (s)	Recoat Speed (mm/s)	Bed Temp. (°C)	Roller Speed (rpm)	Roller Trav. Speed (mm/s)	Ultrasonic Intensity (%)	Roughing Roller Speed (rpm)	Layer Thickness (µm)
UNI-20	90	10	75	400	65	200	80	75	400	40
UNI-10			30	200			10			20
TRI-90										
TRI-70	70									

The green body density of binder jetted alumina parts is intricately influenced by various printing parameters.

The main parameters considered in this research are; binder set time, drying time, recoat speed, roller speed, and roller traverse speed. The binder saturation level exhibits negligible influence on the green densities, given that a substantial portion of the binder undergoes evaporation throughout the curing process. This can also be observed between the TRI-90 and TRI-70 samples wherein the difference in relative density is just 3%. It is approximated that the weight percentage of the binder constitutes less than 1% of the total mass of the green part [19]. The binder set time is the time the binder takes to set after application through the printhead, which influences the consolidation of powder layers. If the binder set time is prolonged, it may lead to increased absorption of the liquid binder into the powder layers before solidification. Therefore, a proper adjustment of the binder set time was made to avoid any smearing in the powder bed which occurs when the rollers spread the powder. The drying time is crucial for ensuring that the printed layers are sufficiently dry before the application of the next layer. Proper drying contributes to the formation of a compact and dense green body. High drying times in a binder jetting process can potentially contribute to layer pushing or powder compaction issues in the powder bed. When the drying time is excessive, it may lead to over-drying of the powder layers. This can result in increased adhesion between the particles, making them more prone to sticking together and forming agglomerates. The over-dried or excessively compacted powder layers may resist the penetration of the binder in subsequent printing layers. As a result, the new powder layers might encounter increased resistance, leading to a pushing or packing effect rather than proper layering resulting in a distorted green body with poor density. The recoat speed is the speed at which subsequent layers are added which impacts the uniform distribution of the powder. A high recoat speed results in insufficient time for the powder to evenly settle and spread across the build area before the next layer is added. This can lead to inadequate powder consolidation and uneven layer thickness which yields a distorted green body and can introduce higher porosity, weak interlayer bonding, and incomplete filling of voids.

Controlling the bed temperature is essential to modulate powder flowability and binder bonding. A bed temperature of 70°C was initially used, however, it made the powder bed wetter as it increased the absorption of the liquid binder into the powder bed. This compromised the formation of form well-defined and cohesive layers, therefore it was lowered to 65°C. The roller speed is the speed at which the roller (smooth and rough) moves across the powder bed. It influences the compaction of the powder layers. Excessive roller speed leads to overcompaction of the powder bed which makes it difficult to achieve a uniform layering and can lead to a layer pushing where the powder layers are displaced instead of being compacted causing distortion of the green body. The roller traverse speed is the rate at which the roller moves from one end of the build plate to the other. This parameter is also critical to achieve a consistent green body density. Furthermore, the layer thickness influences the overall green body structure, however, this parameter was not primarily focused on in this project.

Table 4.9: Relative density of the BJP alumina green body

Sample	**L (mm)**	**W (mm)**	**D (mm)**	**Volume ($\mathbf{cm^3}$)**	**Mass (g)**	**Density ($\mathbf{g/cm^3}$)**	**Relative Density (%)**
UNI-20	45.7	4.3	3.5	0.7	1.4	2.0	50.3
UNI-10	45.6	4.2	3.6	0.7	1.5	2.2	55.5
TRI-90	45.7	4.17	3.1	0.6	1.4	2.4	61.3
TRI-70	46.5	4.2	3.2	0.6	1.4	2.3	58.4
Literature	-	-	-	-	-	2.4 [48]	61.2 [48]

From Table 4.9 it can be noted that the initial utilization of 20µm powder (UNI-20) for printing yielded a comparatively lower relative green body density (about 50.3%). The results from Mariani *et al.* suggest that using smaller particle size (approximately 9 µm) yields higher packing density thus improving the green density. This led to a subsequent transition to a 10 µm powder size (UNI-10), resulting in an improved relative green body density (55.5%). The relative density of UNI-10 was lower when compared to the values presented by Mariani *et al.* (61.2%). This small difference could be due to the use of a smaller powder size by Mariani *et al.* [48]. A study by Du *et al.* demonstrated that the particle size distribution of the feedstock powder has an impact on both the packing density of the powder and the resulting sintered density. Their study suggests that mixing of various powder sizes can fine-tune the PSD thus resulting in a higher green and sintered body density [20]. This led to the further refinement of the powder batch which involved the formulation of a trimodal mixture, incorporating powders of 10 µm, 5 µm, and 2 µm mixed at equal concentrations. The trimodal batch was further differentiated into two subsets, characterized by 90% (TRI-90) and 70% (TRI-70) binder saturation levels. It can be observed that the 90% binder saturation sample exhibited a slightly higher green body density (61.3%) compared to its counterpart with 70% binder saturation (58.4%) suggesting that the binder saturation does not have a huge effect in achieving a higher green body density. This composite mixture demonstrated notably higher green body density values compared to those reported in existing literature studies [48, 20, 47].

Environmental conditions such as weather and humidity, exert substantial influence on the powder bed in binder jet printing processes [31]. Elevated humidity levels cause adverse effects on powder flowability, prompting particle clumping and agglomeration. This was typically observed while trying to replicate the TRI-90 print samples. When the weather and humidity changed (Temperature: 25°C → 18°C; Humidity: 37% → 52%) the print bed quality started deteriorating by forming agglomeration and causing caking. The powder seemed to have absorbed a lot of moisture and it was required to further dry the trimodal batch of powder to remove the moisture. This phenomenon, attributed to moisture absorption, compromises the uniformity of layer deposition and, consequently, the overall quality of the printed part. Furthermore, fluctuations in humidity can impact electrostatic charging behaviors, influencing the cohesion of powder particles and the formation of undesirable agglomerations [68]. Alumina as a material is hydrophilic in nature which suggests that it has a high affinity to water [4]. This makes it difficult during humid days as alumina tends to absorb moisture from the air which alters the surface chemistry and causes poor flowability during the printing process. To mitigate these challenges, the environmental conditions have to be effectively controlled in order to achieve consistent and high-quality prints (densification) during BJP.

4.6.2 Effect of Sintering Conditions on Density

Sintering conditions play a vital role in determining the final densification of the printed alumina parts. The sintering temperature and the holding time (sintering time) are major factors in particle fusion. An adequate holding time facilitates effective material transport and grain boundary diffusion, thereby enhancing overall density [75]. During the debinding process, the binder present in the green body is evaporated through the sintering furnace and this leaves a void between the particles giving room for the fusion of particles to occur. Given that the weight percentage of the binder constitutes only 1% of the total mass [19], a comparatively shorter holding time at the debinding temperature was selected as it impacts the evolution of pore structures within the body. Various sintering parameters were employed during the course of this research, however, the one that yielded the highest densification was selected and shown in Table 4.10. After a particular stage in this research, the sintering parameters were kept constant to see the effect of the printing parameters on the density of the alumina parts. The green bodies with the highest density from each material type were selected to be sintered in the same condition.

Table 4.10: Sintering parameters used for the BJP alumina samples

Sample	**Debinding 1 Temperature (°C)**	**Debinding 1 Time (hrs)**	**Debinding 2 Temperature (°C)**	**Debinding 2 Time (hrs)**	**Sintering Temperature (°C)**	**Sintering Time (hrs)**
UNI-20 UNI-10 TRI-90 TRI-70	600	3	1000	2	1650	24

Although the sintering conditions were constant for the four material types, the final density it yields is different for each material as seen in Table 4.11 and Table 4.12. Table 4.11 shows the relative density of the sintered body which was determined using the geometric method and Table 4.12 shows the relative density of the sintered body which was determined using the buoyancy method. In both methods, UNI-20 showed the least densification (54.06%) as expected from the particle sizes, it can also be seen that the green body density of the UNI-20 sample is also the least when compared to the other material types, however, it increased from a green body density of 50.3% to a sintered body density of 54.1%. The compactness in the green body also promotes grain growth in the alumina samples during sintering, this can be observed in the microstructure figures below. UNI-10 sample showed an improvement in densification, it had a green body densification of 55.5%, however, the sintered body had a relative density of 56.7%. This improvement is not significant which could be due to the lower powder packing efficiency in the BAK-10 powder. TRI-90 samples showed an improvement from a green body density of 61.3% to a sintered body density of 66.9% which is the highest densification achieved when compared to the other scientific works [48, 20, 47]. This is attributed to the better packing efficiency in the trimodal mixture. Finally, the TRI-70 sample showed minor improvements from the green body density to the sintered body density, increasing from 58.4% to 61.1% respectively which is not as much as the TRI-90 sample, suggesting that the binder saturation levels do not play a major role in achieving high-density alumina.

Table 4.11: Relative density of the sintered BJP alumina part using geometric method

Sample	**L (mm)**	**W (mm)**	**D (mm)**	**Volume (cm^3)**	**Mass (g)**	**Density (g/cm^3)**	**Relative Density (%)**
UNI-20	45.2	4.2	3.1	0.6	1.2	2.1	54.1
UNI-10	44.9	4.1	3.5	0.6	1.4	2.2	56.7
TRI-90	44.2	4.0	3.0	0.5	1.4	2.6	66.9
TRI-70	45.6	4.	3.2	0.6	1.4	2.4	61.1
Literature	-	-	-	-	-	2.61 [20]	66.1 [20]

The relative densities determined using the buoyancy method, seen in Table 4.12 show significantly higher values than the relative densities determined using the geometric method (Table 4.11). This significant difference is due to the presence of pores in the sintered alumina parts which affects the volume of the fluid displaced. The porous alumina parts tend to absorb the fluid which fills into the voids left by the binder evaporation post-sintering. Despite their significant inaccuracy, these values exhibit similar trends to those observed in comparable scientific studies. However, it's crucial to note that these values do not provide accurate density values.

Table 4.12: Relative density of the sintered BJP alumina part using buoyancy method

Sample	**Mass (in air) (g)**	**Mass (in water) (g)**	**Density (g/cm^3)**	**Relative Density (%)**
UNI-20	1.2	0.9	3.6	91.0
UNI-10	1.4	1.0	3.7	91.9
TRI-90	1.4	1.1	3.7	95.0
TRI-70	1.4	1.0	3.7	93.4
Literature	-	-	3.7 [47]	93.7 [47]

EDS was performed for all the material types and a clear presence of alumina (aluminum and oxygen elements) was seen on all samples. Slight peaks were observed at the carbon element in between the voids of the alumina particles indicating either the carbon coating made on top of the samples for enabling good picture quality under SEM or the presence of resin from embedding the sample. XRD was also performed on the sintered samples and a clear indication of α-alumina phase can be seen on all the samples without the presence of any other secondary phases.

Figure 4.8 shows the microstructures seen in the cross-sectional surface of the UNI-20 sample. The figure shows that most particles were successfully sintered and clear necking between particles can be observed. Certain smaller particles were still not fusing with the molten alumina around them indicating that there was an insufficient heat transfer caused due to the packing efficiency of the powder. Sample preparation was very challenging as achieving a flat surface was very difficult as the looser particles that did not sinter kept falling off the cross-sectional surface during grinding and polishing. This is also a result of the insufficient heat transfer.

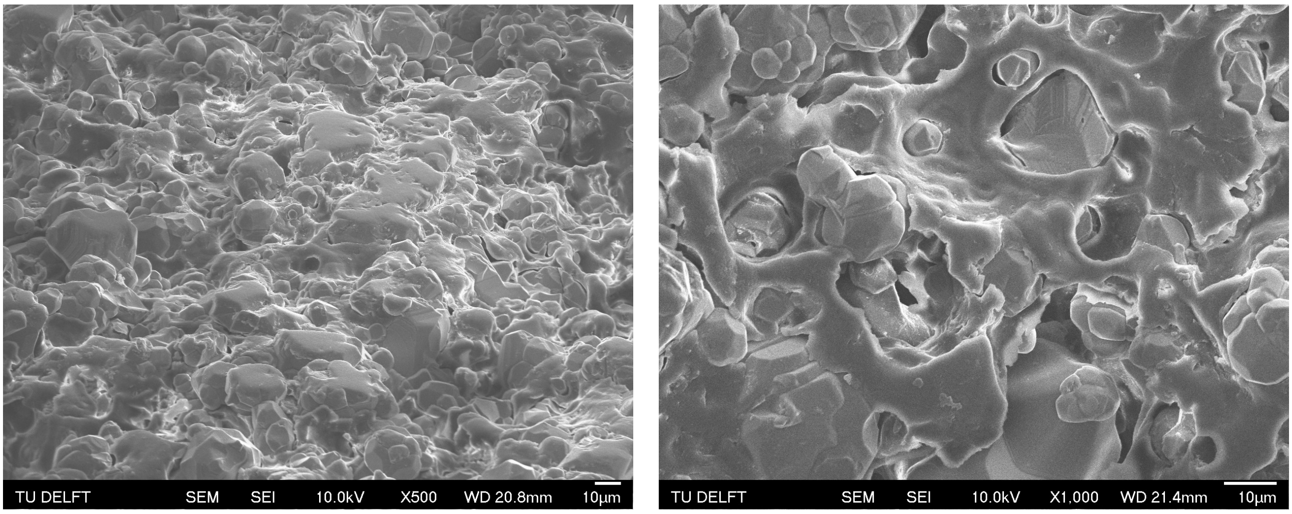

(a) (b)

Figure 4.8: SEM images of the cross-section surface for UNI-20 sample sintered at 1650°C for 24 hours: (a) Overview of the cross-sectional surface, (b) Magnification of fused particles

The alumina particles in the UNI-10 sample were still not sintered completely, even though they had slightly better densification than the UNI-20 sample. The better densification is a result of better packing efficiency when compared to the UNI-20 sample. The microstructure of the cross-sectional surface can be seen in Figure 4.9. The necking between the particles is a lot more prominent in the UNI-10 sample as seen in Figure 4.9. Clear voids left by the evaporated binder can be seen in this sample. Similar to UNI-20 samples, achieving a flat surface during sample preparation was very challenging.

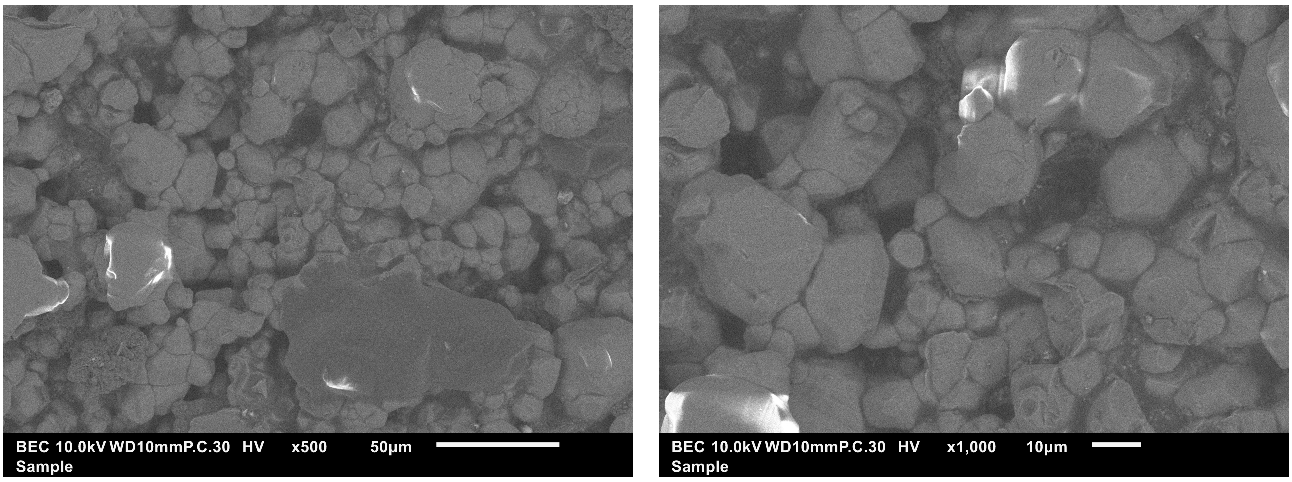

(a) (b)

Figure 4.9: SEM images of the cross-section surface for UNI-10 sample sintered at 1650°C for 24 hours: (a) Overview of the cross-sectional surface, (b) Magnification of fused particles

A clear difference in microstructure can be observed in the TRI-90 samples as seen in Figure 4.10. TRI-90 shows better packing efficiency due to the trimodal mixture, therefore it can be observed that the voids between the coarser particles are filled with finer particles thereby resulting in a higher sintered density. In the case of TRI-90 trimodal mixture, the 5 µm particles fill the voids among the 10 µm particles and the 2 µm particles fill the remaining voids between the 10 µm and 5 µm particles. Figure 4.10 still shows some voids between the fused particles suggesting that further improving the packing efficiency by introducing smaller particles can contribute to achieving an even higher densification. Unlike the UNI-20 and UNI-10 samples, a flatter cross-sectional surface post-grinding and post-polishing was achievable as reflected in Figure 4.10.

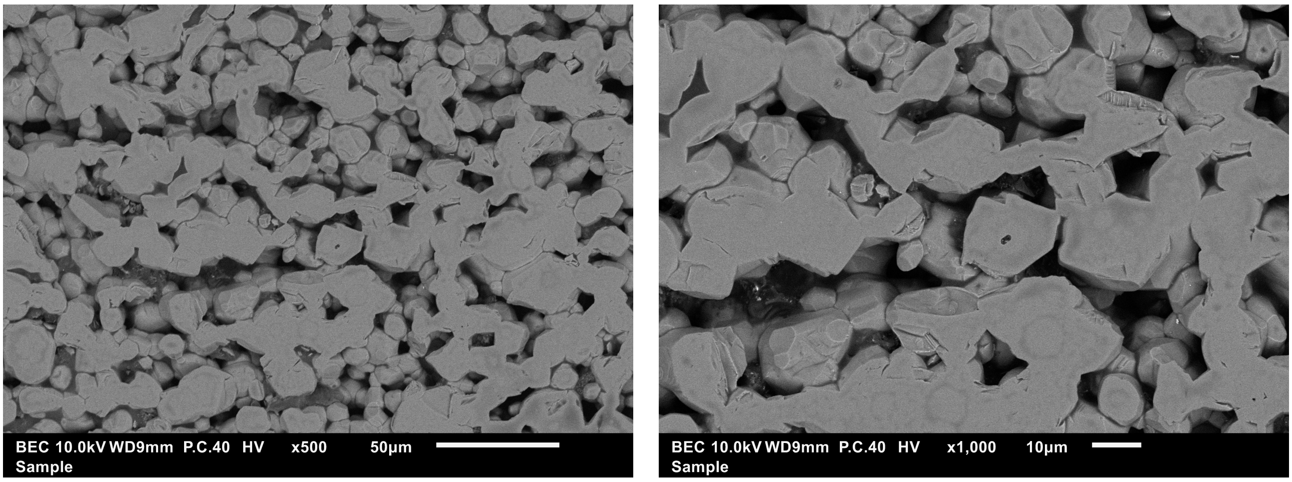

(a) (b)

Figure 4.10: SEM images of the cross-section surface for TRI-90 sample sintered at 1650°C for 24 hours: (a) Overview of the cross-sectional surface, (b) Magnification of fused particles

Figure 4.11 shows the SEM image of the microstructures seen in the cross-sectional area of the TRI-70 sample. The TRI-70 sample has a closer resemblance to the TRI-90 sample as seen in Figure 4.11. TRI-70 samples show a slightly larger presence of voids (filled by resin during sample preparation) which is justifiable given that the densification of the TRI-70 sample is much closer to the TRI-90 sample. Similar to the TRI-90 sample a flatter cross-sectional surface was easily achievable during sample preparation.

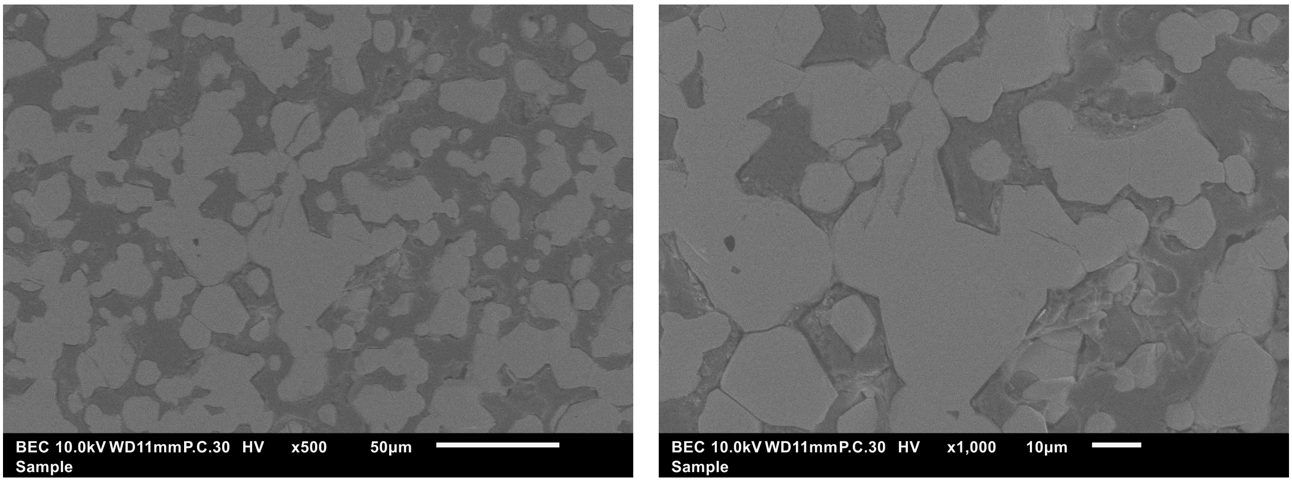

(a) (b)

Figure 4.11: SEM images of the cross-section surface for TRI-70 sample sintered at 1650°C for 24 hours: (a) Overview of the cross-sectional surface, (b) Magnification of fused particles

Shrinkage

The shrinkage from the green body to the sintered body of each of the material types is documented in Table 4.13. Shrinkage was calculated using Equation 4.1:

$$Shrinkage = (\frac{d_i - d_f}{d_i}) * 100 \quad [2] \tag{4.1}$$

Where:
d_i → Initial dimension
d_f → Final dimension

Table 4.13: Shrinkage of sintered BJP alumina parts

Sample	**L** (%)	**W** (%)	**D** (%)
UNI-20	1.1	3.3	12.0
UNI-10	1.6	2.0	2.1
TRI-90	3.2	3.7	5.0
TRI-70	2.7	2.2	2.5
Literature	5.5 [48]	5.5 [48]	8.0 [48]

From these values, it can be observed that the shrinkage mostly happens in the Z direction (X: length; Y: width; Z: Depth) which is slightly lower when compared to other scientific works [48, 20], this is due to various factors that are different than the ones used in this research (particle size, printed part shape, *etc*). The UNI-20 sample showed the most shrinkage in the Z-direction with about 12.0% which is due to the presence of larger pores when compared to the other samples. The shrinkage values are generally lower in the binder jetting technique as seen in Table 4.13. The smaller shrinkage rate suggests that there is sufficient thermal energy provided during sintering which promotes viscous flow and bulk diffusion between alumina particles [48]. The neck growths between the smaller particles as seen in the microstructures above also contribute to the smaller shrinkage trend seen in these samples.

4.7 Mechanical Testing of Binder Jet Printed Alumina

Three-point bending stress was performed only on the sintered TRI-90 and TRI-70 samples featuring a final average density of 66.9% and 61.1%. The other samples (UNI-20 and UNI-10) had very low density to perform the test. Figure 4.12 shows the force vs the extensometer displacement determined for the seven TRI-90 samples. The average load at which the TRI-90 samples break is approximately 32 N.

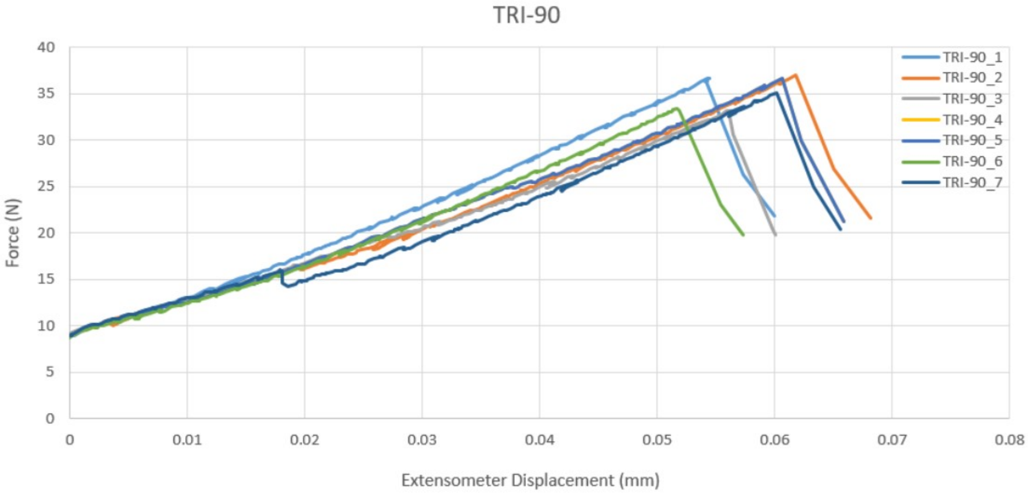

Figure 4.12: Experimental Young's modulus for TRI-90 samples

Figure 4.13 shows the force vs the extensometer displacement determined for the seven TRI-70 samples. The average load at which the conventional part breaks is approximately 18.5 N.

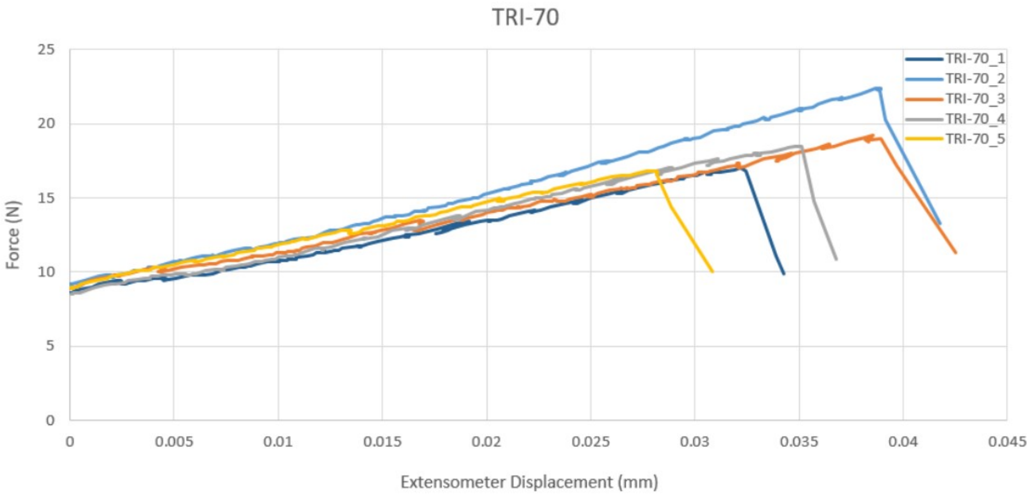

Figure 4.13: Experimental Young's modulus for TRI-70 samples

The mechanical properties of these samples are shown in Table 4.14.

Table 4.14: Young's modulus and flexural stress of BJP alumina samples

Sample	**Gradient (m) (N/mm)**	**Young's Modulus (GPa)**	**Flexural Strength (MPa)**
TRI-90	504.3 ± 34.7	77.3 ± 4.9	59.5 ± 3.2
TRI-70	309.6 ± 42.1	40.1 ± 5.5	28.2 ± 3.4
Literature	-	113 ± 5 [49]	56.1 ± 11.3 [48]

The average Young's modulus and flexural strength for the TRI-90 is 77.3 ± 4.9 GPa and 59.5 ± 3.2 MPa. These values are comparable to those obtained by the three-point bending tests by Mariani *et al.* (9 µm powder) [48] and the four-point bending tests by Melcher *et al.* (0.8 µm powder) [49]. The variation in Young's modulus values between this study and the literature arises from different testing techniques. The literature employs a four-point bending test [49], leading to distinct stress distribution in the material during testing, with stress concentration covering a larger region. A significant difference was observed between the conventional sample values and the binder jetted samples. This difference is primarily due to the difference in densification (98.5% vs 66.9% and 61.1%). The Young's modulus values of the TRI-90 samples are approximately five times lower than the conventional samples, while the flexural strength is ten times. TRI-70, on the other hand, exhibits half the values of the TRI-90 samples. The reduced strength results from the presence of pores and imperfections, which amplifies stress in certain areas, increasing the likelihood of crack propagation [48].

CHAPTER 5

CONCLUSIONS

This research explores the additive manufacturing of high-purity alumina samples (99.9%) using the binder jetting printing (BJP) technique. The goal of this research is to achieve high densification alumina parts which would serve as a basis to fabricate ASML's reticle masking blades that are used in their EUV lithography machines. Four different powder particle sizes were used; 20 µm, 10 µm, 5 µm, and 2 µm. The research initially used an unimodal composition of the 20 µm and 10 µm (UNI-20 and UNI-10). Later a trimodal composition of the 10 µm, 5 µm, and 2 µm was used as two different material types, one with 90% binder saturation (TRI-90) and the other with 70% binder saturation (TRI-70). A conventional alumina sample with a relative density of 98.6% was considered as a reference material to understand the differences in the microstructure and mechanical properties.

The following conclusions can be made based on the research objectives:

- Material and Design Optimization:
  - The material selection process resulted in three options that had superior properties when compared to stainless steel 316L: siliconized silicon carbide, aluminum nitride, and alumina. Alumina was ultimately chosen due to its widespread availability and cost-effectiveness among the three materials.
  - An optimized design was made to be fabricated as one piece using the BJP. Thermo-mechanical simulations were performed on the optimized design assuming a 100% densification of alumina. The simulations validate the necessity of incorporating cooling channels to ensure an effective flow of temperature within the blade. The simulations showed temperatures and stress distribution below the allowed maximum boundaries per ASML's requirements. However, the porosity in the binder jetted alumina samples affects the integrity of the entire blade assembly.
- Process Optimization:
  - Optimal printing and sintering parameters were chosen from a range of options, resulting in the highest green body and sintered body density.
  - The green body density is directly proportional to the sintered body density which correlates to the packing efficiency of the powder bed. The TRI-90 samples showed the highest green body density (61.3%) and the highest sintered density (66.9%) which is the highest observed when compared to other scientific works.
  - Using a combination of coarser and finer particles results in high green body densification as the finer particles fill the voids present between the coarser particles.
  - Environmental conditions such as weather and humidity impact the powder bed quality making it difficult to achieve consistent print quality.
- Functional Optimization:
  - Shrinkage rates in all directions are approximately 3-5%, suggesting the possibility of achieving highly accurate printed parts.

  - Lower sintered density yields lower mechanical properties. The TRI-90 samples yielded the highest Young's modulus value of 77.3 GPa and the highest flexural strength value of 59.5 MPa. These values are comparable to the values obtained in other scientific works.

5.1 Recommendations

Based on the conclusions seen above, various recommendations can be made for improving the densification of alumina:

- Material and Design Optimization:
  - Particle size: The findings of this research substantiate the influence of particle size on powder bed density, subsequently affecting the sintered density of alumina particles. Future investigations could extend this research by employing an unimodal powder distribution with particle sizes of 5 µm and 2µm powder. This comparative analysis aims to discern density disparities in relation to the UNI-20 and UNI-10 powder batches.
  - Particle size distribution: The influence of PSD can be further investigated through the utilization of smaller powder particles compared to those employed in the TRI-90 batch. For instance, employing a multimodal combination of particles with sizes 7 µm, 5 µm, and 2 µm could serve as an initial exploration. Moreover, determining the optimal mixing fraction and packing density is crucial for the attainment of high-density alumina. A study conducted by Du *et al.* employed the discrete element method (DEM) to model powder packing, providing a valuable approach to determining the optimal concentrations of the multimodal powder batch [20].
  - Sintering additives: Incorporating sintering additives enhances the material properties of alumina. The introduction of optimal concentrations of these additives contributes to heightened densification of alumina particles, consequently leading to improved mechanical properties. In a study conducted by Yu *et al.* the utilization of $Ca(OH)_2$-MgO-SiO_2 as a sintering additive in the fabrication of alumina ceramics which resulted in a density of 83.3% [76].
  - Nanoparticle densifiers: Nanoparticle densifiers have the potential to enhance the properties of binders when introduced in varying concentrations. This approach not only holds promise for achieving heightened densification but also for augmenting the mechanical characteristics of the resulting material. A study conducted by Kunchala *et al.* incorporated alumina nanoparticles with a particle size below 50 nm. This integration resulted in a notable 30% increase in densification and a substantial 740% improvement in compressive strength compared to samples devoid of such densifiers [40]. The findings strongly indicate that the nanoparticles within the binders effectively occupied the interparticle void spaces among the finer particles, yielding encouraging outcomes.
  - Hot isostatic pressing (HIP): In the HIP technique, heat, and pressure are applied isostatically. This method proves effective in enhancing the densification of alumina samples. A notable disparity in both densification and mechanical properties is evident when comparing the outcomes of conventional samples with those produced through binder jetting in this research. This technique can be beneficial in elevating densification and augmenting the mechanical characteristics of binder jetted alumina.
- Process Optimization:
  - Environmental conditions: This research also clearly indicates that environmental conditions, such as weather and humidity, have a noticeable impact on the quality of the powder bed. To mitigate these effects, incorporating an environmental control chamber around the printer can be advantageous. This chamber helps eliminate external factors, such as weather and humidity, thereby aiding in the attainment of improved powder bed quality.
- Functional Optimization:
  - Once a densification level of 90% or higher is reached, more attention can be directed toward meeting ASML's grade 1 cleanliness standards. This involves conducting outgassing tests to evaluate the release of any volatile substances or gases from the material under ASML's specific conditions, including vacuum or elevated temperature. It is also crucial to prioritize achieving higher dimensional accuracy during this phase.
  - It is crucial to emphasize the coating of the ceramic blade to ensure it meets the necessary electrical and optical properties for the production of the final REMA blade.

BIBLIOGRAPHY

[1] Admin. *What is Moore's law and why is it so great?* Feb. 2019. URL: https://www.semiconductors.org/what-is-moores-law-and-why-is-it-so-great/#:~:text=Moore%5C%E2%5C%80%5C%99s%5C%20Law%5C%20has%5C%20enabled%5C%20the%5C%20semiconductor%5C%20industry%5C%20to,economy%5C%20typically%5C%20increases%5C%20over%5C%20time%5C%20due%5C%20to%5C%20inflation..

[2] Siti Salwa Alias, Zawati Harun, and Nur Farhani Ismail. "Microstructure and physical characterization of alumina-sintered body via hot isostatic pressing". In: *Journal of the Australian Ceramic Society* 55 (4 Dec. 2019), pp. 969–975. ISSN: 25101579. DOI: 10.1007/s41779-019-00308-8.

[3] Pertti. Auerkari. *Mechanical and physical properties of engineering alumina ceramics*. Technical Research Centre of Finland, 1996.

[4] Min A. Bae, Kyeong Ho Kim, and Jae Ho Baek. "Effect of the Properties of Binder and Powder Used in Binder Jet 3D Printing on Build-Up". In: *International Journal of Metalcasting* (Oct. 2023). ISSN: 21633193. DOI: 10.1007/s40962-023-01014-9.

[5] Y. Baik and R. A.L. Drew. "Aluminum nitride: Processing and applications". In: *Key Engineering Materials* (122-124 1996). ISSN: 16629795. DOI: 10.4028/www.scientific.net/kem.122-124.553.

[6] Vivek Bakshi. "EUV lithography". In: (2009).

[7] Michel W. Barsoum. *Fundamentals of Ceramics*. 2nd ed. CRC Press, Dec. 2019. ISBN: 9781498708166. DOI: 10.1201/9781498708166. URL: https://www.taylorfrancis.com/books/9781000357219.

[8] B Ben-Nissan, A H Choi, and R Cordingley. "10 - Alumina ceramics". In: *Bioceramics and their Clinical Applications* (2008). Ed. by Tadashi Kokubo, pp. 223–242. DOI: https://doi.org/10.1533/9781845694227.2.223. URL: https://www.sciencedirect.com/science/article/pii/B9781845692049500107.

[9] Garry J Bordonaro. "DUV Photolithography and Materials". In: *Encyclopedia of Nanotechnology* (2012). Ed. by Bharat Bhushan, pp. 590–604. DOI: 10.1007/978-90-481-9751-4_370. URL: https://doi.org/10.1007/978-90-481-9751-4_370.

[10] C. Barry Carter and M. Grant Norton. *Ceramic Materials: Science and Engineering*. 2nd ed. Springer New York, Jan. 2013, pp. XXXIII–766. ISBN: 978-1-4614-3522-8. DOI: 10.1007/978-1-4614-3523-5. URL: https://link.springer.com/10.1007/978-1-4614-3523-5.

[11] Christian Cavallo. *All about binder jetting 3D printing*. July 2020. URL: https://www.thomasnet.com/articles/custom-manufacturing-fabricating/all-about-binder-jetting-3d-printing/#:~:text=Binder%5C%20jetting%5C%20is%5C%20a%5C%20family%5C%20of%5C%20additive%5C%20manufacturing,powder%5C%20in%5C%20the%5C%20shape%5C%20of%5C%20a%5C%20part%5C%20layer.

[12] Y.C. Chan and J.P. Singh. "Columnar grain growth in ceramics". In: *Journal of the American Ceramic Society* 80.1 (1997), pp. 3–14.

[13] Gregory Mbanaso Chimaobi and Denbeaux. *EUV Lithography*. Ed. by Bharat Bhushan. Springer Netherlands, 2012, pp. 797–803. ISBN: 978-90-481-9751-4. DOI: 10.1007/978-90-481-9751-4_391. URL: https://doi.org/10.1007/978-90-481-9751-4_391.

[14] J. B. Clark and J. S. Vickers. "Lamellar structure in ceramics". In: *Journal of the American Ceramic Society* 65.5 (1982), pp. C-89-C–91.

[15] DAVID R. CLARKE. "On the Equilibrium Thickness of Intergranular Glass Phases in Ceramic Materials". In: *Journal of the American Ceramic Society* 70 (1 Jan. 1987), pp. 15–22. ISSN: 0002-7820. DOI: 10.1111/j.1151-2916.1987.tb04846.x.

[16] Robert Danzer et al. "Fracture of ceramics". In: *Advanced Engineering Materials* 10 (4 Apr. 2008), pp. 275–298. ISSN: 14381656. DOI: 10.1002/adem.200700347.

[17] Lutgard C De Jonghe and Mohamed N Rahaman. "4.1 sintering of ceramics". In: *Handbook of advanced ceramics: materials, applications, processing and properties* 2 (2003), p. 187.

[18] Fahimeh Dini et al. "A review of binder jet process parameters; powder, binder, printing and sintering condition". In: *Metal Powder Report* 75 (2 Mar. 2020), pp. 95–100. ISSN: 18734065. DOI: 10.1016/j.mprp.2019.05.001.

[19] Truong Do, Patrick Kwon, and Chang Seop Shin. "Process development toward full-density stainless steel parts with binder jetting printing". In: *International Journal of Machine Tools and Manufacture* 121 (Oct. 2017), pp. 50–60. ISSN: 08906955. DOI: 10.1016/j.ijmachtools.2017.04.006.

[20] Wenchao Du et al. "Binder Jetting Additive Manufacturing: Effect of Particle Size Distribution on Density". In: *Journal of Manufacturing Science and Engineering, Transactions of the ASME* 143 (9 Sept. 2021). ISSN: 15288935. DOI: 10.1115/1.4050306.

[21] J. Martínez Fernández et al. "Microstructure-mechanical properties correlation in siliconized silicon carbide ceramics". In: *Acta Materialia* (11 June 2003). ISSN: 13596454. DOI: 10.1016/S1359-6454(03)00157-5.

[22] Lorraine F. Francis. *Powder Processes*. Elsevier, Jan. 2016, pp. 343–414. ISBN: 9780123851321. DOI: 10.1016/B978-0-12-385132-1.00005-7.

[23] Nan Fu et al. "EUV Lithography: State-of-the-Art Review". In: *Journal of Microelectronic Manufacturing* 2 (2 2019), pp. 1–6. ISSN: 2578-3769. DOI: 10.33079/jomm.19020202. URL: http://www.jommpublish.org/p/29/.

[24] Gangfeng Guo et al. "Direct measurement of residual stresses and their effects on the microstructure and mechanical properties of heat-treated Si3N4 ceramics". In: *Acta Materialia* 54 (9 May 2006), pp. 2311–2316. ISSN: 13596454. DOI: 10.1016/j.actamat.2005.12.011.

[25] Ashutosh Kumar Gupta, Krishnanand, and Mohammad Taufik. "The effect of process parameters in material extrusion processes on the part surface quality: A review". In: *Materials Today: Proceedings* 50 (2021), pp. 1234–1242. ISSN: 22147853. DOI: 10.1016/j.matpr.2021.08.110.

[26] Frank Händle. *Extrusion in ceramics*. Springer Science & Business Media, 2007.

[27] Richard van Haren et al. "The impact of the reticle and wafer alignment mark placement accuracy on the intra-field mask-to-mask overlay". In: *Photomask Japan 2019: XXVI Symposium on Photomask and Next-Generation Lithography Mask Technology*. Vol. 11178. SPIE. 2019, pp. 200–211.

[28] Jonathan H Harris. "Sintered aluminum nitride ceramics for high-power electronic applications". In: *JOM* (1998).

[29] Craig Higgins et al. "Integration of an EUV metal layer: a 20/14nm demo". In: *Extreme Ultraviolet (EUV) Lithography V*. Vol. 9048. SPIE. 2014, pp. 449–457.

[30] M. Jabbari et al. "Ceramic tape casting: A review of current methods and trends with emphasis on rheological behaviour and flow analysis". In: *Materials Science and Engineering B: Solid-State Materials for Advanced Technology* 212 (Oct. 2016), pp. 39–61. ISSN: 09215107. DOI: 10.1016/j.mseb.2016.07.011.

[31] Alireza Jalili. *A closer look for binder jet printer: How it works and what makes it unique*. May 2023. URL: https://theadditivemanufacturing.com/binder-jet-printer/.

[32] The Ceramic Society of Japan. *Advanced Ceramic Technologies & Products*. 1st ed. Springer Japan, Oct. 2012, pp. XV–585. ISBN: 978-4-431-53913-1. DOI: 10.1007/978-4-431-54108-0. URL: http://link.springer.com/10.1007/978-4-431-54108-0.

[33] Edgar Mendoza Jimenez et al. "Parametric analysis to quantify process input influence on the printed densities of binder jetted alumina ceramics". In: *Additive Manufacturing* 30 (Dec. 2019). ISSN: 22148604. DOI: 10.1016/j.addma.2019.100864.

[34] Perrine Juillion. *What is equiaxed structure?* Oct. 2019. URL: https://studybuff.com/what-is-equiaxed-structure/.

[35] W David Kingery, Harvey Kent Bowen, and Donald R Uhlmann. *Introduction to ceramics*. Vol. 17. John wiley & sons, 1976.

[36] F Kools and O Fiquet. "Wet Pressing for Forming Advanced Ceramics". In: *Science and technology of ferrite magnets: modeling of coercivity and grain growth inhibition* (1989), p. 103.

[37] Dimitri Kopeliovich. *Materials engineering*. Nov. 2014. URL: `https://www.substech.com/dokuwiki/doku.php?id=sintering_of_ceramics#:~:text=Sintering%5C%20(Firing)%5C%20of%5C%20ceramic%5C%20materials,to%5C%20the%5C%20neghbouring%5C%20powder%5C%20particles.`.

[38] Dmitri Kopeliovich. *Materials engineering*. May 2012. URL: `https://www.substech.com/dokuwiki/doku.php?id=methods_of_shape_forming_ceramic_powders`.

[39] Carolin Körner et al. "Tailoring the grain structure of IN718 during selective electron beam melting". In: vol. 14. EDP Sciences, 2014. DOI: `10.1051/matecconf/20141408001`.

[40] Pragnya Kunchala and Keerti Kappagantula. "3D printing high density ceramics using binder jetting with nanoparticle densifiers". In: *Materials and Design* 155 (Oct. 2018), pp. 443–450. ISSN: 18734197. DOI: `10.1016/j.matdes.2018.06.009`.

[41] Y Lakhdar et al. "Additive manufacturing of advanced ceramic materials". In: *Progress in Materials Science* 116 (2021), p. 100736. ISSN: 0079-6425. DOI: `https://doi.org/10.1016/j.pmatsci.2020.100736`. URL: `https://www.sciencedirect.com/science/article/pii/S0079642520301006`.

[42] B. R. Lawn, A. G. Evans, and D. B. Marshall. "Elastic/Plastic Indentation Damage in Ceramics: The Median/Radial Crack System". In: *Journal of the American Ceramic Society* 63 (9-10 1980), pp. 574–581. ISSN: 15512916. DOI: `10.1111/j.1151-2916.1980.tb10768.x`.

[43] F Lemoisson and L Froyen. *12 - Understanding and improving powder metallurgical processes*. Ed. by Seshadri Seetharaman. Woodhead Publishing, 2005, pp. 471–502. ISBN: 978-1-85573-927-7. DOI: `https://doi.org/10.1533/9781845690946.2.471`. URL: `https://www.sciencedirect.com/science/article/pii/B9781855739277500121`.

[44] W A Lewis Jr. "Dry pressing technical ceramics". In: *American Ceramic Society Bulletin* 75.4 (Apr. 1996). URL: `https://www.osti.gov/biblio/247990`.

[45] Horng-Hwa Lu and Jow-Lay Huang. *Effect of Y2O3 and Yb2O3 on the microstructure and mechanical properties of silicon nitride*. 2001. URL: `www.elsevier.com/locate/ceramint`.

[46] V. Mamedov. "Spark plasma sintering as advanced PM sintering method". In: *Powder Metallurgy* 45 (4 2002), pp. 322–328. ISSN: 00325899. DOI: `10.1179/003258902225007041`.

[47] Supalak Manotham and Passakorn Tesavibul. "Effect of particle size on mechanical properties of alumina ceramic processed by photosensitive binder jetting with powder spattering technique". In: *Journal of the European Ceramic Society* 42 (4 Apr. 2022), pp. 1608–1617. ISSN: 1873619X. DOI: `10.1016/j.jeurceramsoc.2021.11.062`.

[48] Marco Mariani et al. "3D printing of fine alumina powders by binder jetting". In: *Journal of the European Ceramic Society* 41 (10 2021), pp. 5307–5315. ISSN: 0955-2219. DOI: `https://doi.org/10.1016/j.jeurceramsoc.2021.04.006`. URL: `https://www.sciencedirect.com/science/article/pii/S0955221921002466`.

[49] Reinhold Melcher et al. "3D printing of Al2O3/Cu-O interpenetrating phase composite". In: *Journal of Materials Science* 46 (5 Mar. 2011), pp. 1203–1210. ISSN: 00222461. DOI: `10.1007/s10853-010-4896-3`.

[50] Gordon E Moore et al. *Cramming more components onto integrated circuits*. 1965.

[51] Lalit M Pandey and Rushikesh Fopase. *Nanoscale Engineering of Biomaterials: Properties and Applications*. Springer, 2022.

[52] PTI. *Ceramic Injection Molding*. URL: `http://polymertek.com/inject/ceramic-mim/process/`.

[53] Mohamed N. Rahaman. *Ceramic Processing and Sintering*. 2nd ed. Materials engineering 23. M. Dekker, 2003. ISBN: 9780824709884.

[54] Dr. Frank Rohmund. *So does EUV lithography work*. Dec. 2022. URL: `https://www.zeiss.com/semiconductor-manufacturing-technology/smt-magazine/so-does-euv-lithography-work.html`.

[55] Kurt Ronse. "Optical lithography—a historical perspective". In: *Comptes Rendus Physique* 7 (8 2006). Ultimate lithography, pp. 844–857. ISSN: 1631-0705. DOI: `https://doi.org/10.1016/j.crhy.2006.10.007`. URL: `https://www.sciencedirect.com/science/article/pii/S1631070506002192`.

[56] David Rosen et al. *Additive Manufacturing Technologies*. Springer International Publishing, 2021. ISBN: 978-3-030-56129-1. DOI: `10.1007/978-3-030-56127-7`. URL: `https://link.springer.com/10.1007/978-3-030-56127-7`.

[57] M Roy, A Bandyopadhyay, and S Bose. “Chapter 6 - Ceramics in Bone Grafts and Coated Implants”. In: ed. by Susmita Bose and Amit Bandyopadhyay. Academic Press, 2017, pp. 265–314. ISBN: 978-0-12-802792-9. DOI: `https://doi.org/10.1016/B978-0-12-802792-9.00006-9`. URL: `https://www.sciencedirect.com/science/article/pii/B9780128027929000069`.

[58] David Salamon. “Advanced Ceramics”. In: *Advanced Ceramics for Dentistry* (2014). DOI: `10.1016/B978-0-12-394619-5.00006-7`.

[59] Jan van Schoot et al. “High-NA EUV lithography exposure tool progress”. In: ed. by Kenneth A Goldberg. Vol. 10957. SPIE, 2019, p. 1095707. DOI: `10.1117/12.2515205`. URL: `https://doi.org/10.1117/12.2515205`.

[60] Zhijian Shen et al. “Spark plasma sintering of alumina”. In: *Journal of the American Ceramic Society* 85 (8 2002), pp. 1921–1927. ISSN: 00027820. DOI: `10.1111/j.1151-2916.2002.tb00381.x`.

[61] Valmir José da Silva et al. “Refractory ceramics of clay and alumina waste”. In: *Materials Research* 24 (2 2021). ISSN: 19805373. DOI: `10.1590/1980-5373-MR-2020-0485`.

[62] Jungchul Song, Chae-Hwan Kim, and Ga-Won Lee. “A Study on the Resolution and Depth of Focus of ArF Immersion Photolithography”. In: *Micromachines* 13 (11 Nov. 2022), p. 1971. DOI: `10.3390/mi13111971`.

[63] Jesper Stjernberg et al. “Laboratory scale study of the degradation of mullite/corundum refractories by reaction with alkali-doped deposit materials”. In: *Ceramics International* 39.1 (2013), pp. 791–800.

[64] M Suleiman et al. “Effect of the powder characteristics on the properties of semi-dry pressed alumina”. In: *Ceramics International* 44.18 (2018), pp. 22833–22840.

[65] S. Sun, Milan Brandt, and M. Easton. “Powder bed fusion processes: An overview”. In: *Laser Additive Manufacturing: Materials, Design, Technologies, and Applications* (2017), pp. 55–77. DOI: `10.1016/B978-0-08-100433-3.00002-6`.

[66] International Syalons. *What is slip casting?* Sept. 2018. URL: `https://www.syalons.com/2018/09/06/slip-casting-sialons/`.

[67] *The Three Point Bend Test*. 2018. URL: `https://mi.eng.cam.ac.uk/IALego/bender_files/bend_theory.pdf`.

[68] Alexander Tkach, Miguel Garcez, and Paula M. Vilarinho. “Electrostatic Charges of Abrasive Powders: The Role of Particle Size and Humidity”. In: *Coatings* 11 (12 Dec. 2021). ISSN: 20796412. DOI: `10.3390/coatings11121520`.

[69] Cekdar Vakifahmetoglu, Tugce Semerci, and Gian Domenico Soraru. “Closed porosity ceramics and glasses”. In: *Journal of the American Ceramic Society* 103 (5 May 2020), pp. 2941–2969. ISSN: 15512916. DOI: `10.1111/jace.16934`.

[70] Djordje Veljović et al. “The effect of grain size on the biocompatibility, cell–materials interface, and mechanical properties of microwave-sintered bioceramics”. In: *Journal of Biomedical Materials Research Part A* 100.11 (2012), pp. 3059–3070.

[71] Daniele Mari (editor) Vinod K. Sarin (editor-in-chief) Luis Llanes (editor). *Comprehensive Hard Materials volume 2 Ceramics*. 1st ed. Vol. 2. Comprehensive Hard Materials. Elsevier, 2014. ISBN: 978-0-444-63384-2.

[72] Zhejun Wang. “Bioceramic materials in endodontics”. In: *Endodontic topics* 32.1 (2015), pp. 3–30.

[73] Amy Wat et al. “Bioinspired nacre-like alumina with a bulk-metallic glass-forming alloy as a compliant phase”. In: *Nature Communications* 10 (1 Dec. 2019). ISSN: 20411723. DOI: `10.1038/s41467-019-08753-6`.

[74] De-Kun Yang et al. “The development of laser-produced plasma EUV light source”. In: *Chip* 1 (3 Sept. 2022), p. 100019. ISSN: 27094723. DOI: `10.1016/j.chip.2022.100019`.

[75] Qingrui Yin, Binghe Zhu, and Huarong Zeng. *Microstructure, Property and Processing of Functional Ceramics*. Trans Tech Publications Ltd, 2010. ISBN: 978-3-642-01693-6.

[76] Tianlin Yu, Ze Zhao, and Junchao Li. “Effect of sintering temperature and sintering additives on the properties of alumina ceramics fabricated by binder jetting”. In: *Ceramics International* 49 (6 Mar. 2023), pp. 9948–9955. ISSN: 02728842. DOI: `10.1016/j.ceramint.2022.11.172`.

[77] Ye Zhang et al. “Microstructure evolution and high-temperature mechanical properties of porous Si3N4 ceramics prepared by SHS with a small amount of Y2O3 addition”. In: *Ceramics International* 47 (4 Feb. 2021), pp. 5656–5662. ISSN: 02728842. DOI: `10.1016/j.ceramint.2020.10.151`.